UNIVERSITAT POLITÈCNICA DE VALÈNCIA

UNIVERSITAT POLITÈCNICA DE VALÈNCIA

Escuela Técnica Superior de Ingeniería Industrial

Diseño de un transductor focalizado de ultrasonidos y evaluación de algoritmos de compensación de respuesta impulsional para un microscopio fotoacústico de resolución óptica

Trabajo Fin de Máster

Máster Universitario en Ingeniería Biomédica

AUTOR/A: Navarro Calvo, Javier Ángel

Tutor/a: Camarena Femenia, Francisco

Cotutor/a: Cebrecos Ruiz, Alejandro

Cotutor/a externo: GARCIA GARRIGOS, JUAN JOSE

CURSO ACADÉMICO: 2022/2023

Acknowledgements

A todos mis compañeros de Lab que han soportado dudas este año,
y las han convertido en tranquilidad.
Y a la que me hace mejor persona, lo cual me hace mejor investigador,
lo cual me hace mejor persona.

Abstract

Optical resolution photoacoustic microscopy (OR-PAM) is an emerging biomedical imaging technique, which combines optical excitation of different absorbing molecules with acoustic detection of the generated ultrasound waves, providing high resolution images of endogenous chromophores such as hemoglobin or melanin. The present work is framed in the creation of the second generation of an OR-PAM prototype, which is based on the use of a low-cost laser source (pulsed laser diode or PLD) to reduce the cost of the system. Because it is oriented to clinical practice, both the image quality and the acquisition time must be optimized. For this purpose, a single-element focused ultrasound transducer has been designed, both its geometry and frequency response, to provide a high-sensitivity detection of the generated low-amplitude photoacoustic signal. In addition, due to the use of a fast laser-scanning method which moves the optical focal spot along the imaging area, the signal suffers strong distortions at off-centered positions away from the transducer sensitivity zone. As a solution, a simulation study has been carried out for the implementation of three impulse response-based algorithms Spatially-Variant Filter (SVF), Spatial Matched Filter (SMF) and Weighted Back-Projection (WBP), analyzing and characterizing their performance in the compensation of this effect. The obtained photoacoustic images show a substantial signal-to-noise ratio improvement, extending the effective field of view of the image by an order of magnitude (from 0.1 to 1 mm^2), which represents a breakthrough in the implementation of competitive and low-cost OR-PAM systems in clinical applications.

Javier A. Navarro Calvo
Contact: janacal@i3m.upv.es

Key Words: OR-PAM, photoacoustic imaging, focused ultrasound transducer, spatial impulse response.

Resumen

La microscopía fotoacústica de resolución óptica (OR-PAM) es una nueva técnica de imagen biomédica, la cual combina la excitación óptica de diferentes moléculas absorbentes con la detección acústica de las ondas de ultrasonidos generadas, ofreciendo imágenes de alta resolución de cromóforos endógenos como la hemoglobina o la melanina. El presente trabajo se enmarca en la creación de la segunda generación de un prototipo OR-PAM, el cual se basa en el uso de una fuente láser de bajo coste (diodo láser pulsado o PLD) para reducir el coste del sistema. Debido a que está orientado a la práctica clínica, tanto la calidad como el tiempo de adquisición de la imagen deben ser optimizados. Para ello, se ha diseñado un transductor de ultrasonidos focalizado monoelemento, tanto la geometría como la respuesta en frecuencia, para proporcionar una detección de alta sensibilidad de la señal fotoacústica de baja amplitud generada. Además, debido al uso de un método de escaneo láser rápido el cual mueve el punto focal óptico a lo largo del área de imagen, la señal sufre fuertes distorsiones en puntos descentrados lejos de la zona de sensibilidad del transductor. Como solución, se ha realizado un estudio de simulación para la implementación de tres algoritmos basados en la respuesta espacial del transductor Spatially-Variant Filter (SVF), Spatial Matched Filter (SMF) y Weighted Back-Projection (WBP), analizando y caracterizando su rendimiento en la compensación de dicho efecto. Las imágenes fotoacústicas obtenidas muestran una mejora sustancial de la relación señal a ruido, ampliando el campo de visión efectivo de la imagen en un orden de magnitud (desde 0.1 hasta 1 mm^2), lo cual supone un gran avance en la implementación de sistemas OR-PAM competitivos y de bajo coste en aplicaciones clínicas.

Javier A. Navarro-Calvo
Contacto: janacal@i3m.upv.es

Palabras Clave: OR-PAM, imagen fotoacústica, transductor de ultrasonidos focalizado, respuesta espacial al impulso .

Resum

La microscòpia fotoacústica de resolució òptica (OR-PAM) és una nova tècnica d'imatge biomèdica, la qual combina l'excitació òptica de diferents molècules absorbents amb la detecció acústica de les ones d'ultrasons generades, oferint imatges d'alta resolució de cromòfors endògens com la hemoglobina o la melanina. Aquest treball s'emmarca en la creació de la segona generació d'un prototip OR-PAM, el qual es basa en l'ús d'una font làser de baix cost (díode làser polsat o PLD) per reduir el cost del sistema. Per la seua orientació a la pràctica clínica, tant la qualitat com el temps d'adquisició de la imatge han de ser optimitzats. Per això, s'ha dissenyat un transductor d'ultrasons focalitzat monoelement, tant la geometria com la resposta en freqüència, per proporcionar una detecció d'alta sensibilitat del senyal fotoacústic de baixa amplitud generada. A més, a causa de l'ús d'un mètode d'escaneig làser ràpid que mou el punt focal òptic al llarg de l'àrea d'imatge, el senyal pateix fortes distorsions en punts descentrats lluny de la zona de sensibilitat del transductor. Com a solució, s'ha realitzat un estudi de simulació per a la implementació de tres algoritmes basats en la resposta al impuls espacial del transductor Spatially-Variant Filter (SVF), Spatial Matched Filter (SMF) i Weighted Back-Projection (WBP), analitzant i caracteritzant el rendiment en la compensació d'aquest efecte. Les imatges fotoacústiques obtingudes mostren una millora substancial de la relació senyal a soroll, ampliant el camp de visió efectiu de la imatge en un ordre de magnitud (des de 0.1 fins a 1 mm^2), la qual cosa suposa un gran avenç en la implementació de sistemes OR- PAM competitius i de baix cost en aplicacions clíniques.

Javier A. Navarro Calvo
Contacte: janacal@i3m.upv.es

Paraules Clau: OR-PAM, imatge fotoacústica, transductor d'ultrasons focalitzat, resposta espacial a l'impuls.

Contents

Part I

Memory

Chapter 1

Introduction

1.1 Photoacoustic imaging

Photoacoustic or optoacoustic imaging (PAI) is an emerging hybrid biomedical imaging modality which combines pulsed laser excitation and ultrasonic detection (Beard, 2011). As its name suggests, it is based on the photoacoustic effect described by Alexander Graham Bell in 1880, who envisioned how acoustic waves could be produced without electricity as modulated sunlight hit a material with variable resistance (Bell, 1880). With technology growth and subsequent invention of lasers and instrumentation electronics, this research was transferred to the biomedical field, gaining special interest over the last two decades. Within this compressed period of time, several research groups have been exploiting their knowledge for the creation of experimental pre-clinical setups for *in-vivo* functional imaging, developing reconstruction algorithms, and continuing to investigate and understand this phenomenon to further improve the technique.

A schematic of the photoacoustic imaging process is shown in Fig. 1.1. When a pulsed laser irradiates a biological tissue, the deposited energy is absorbed by certain molecules in the tissue, called chromophores. For a sufficiently short excitation (ns), a thermoelastic expansion occurs generating acoustic pressure waves in the ultrasonic range that can be detected by an ultrasound transducer, allowing to form an image of the inner tissue chromophores applying reconstruction algorithms to the detected photoacoustic signals (L. V. Wang, 2008).

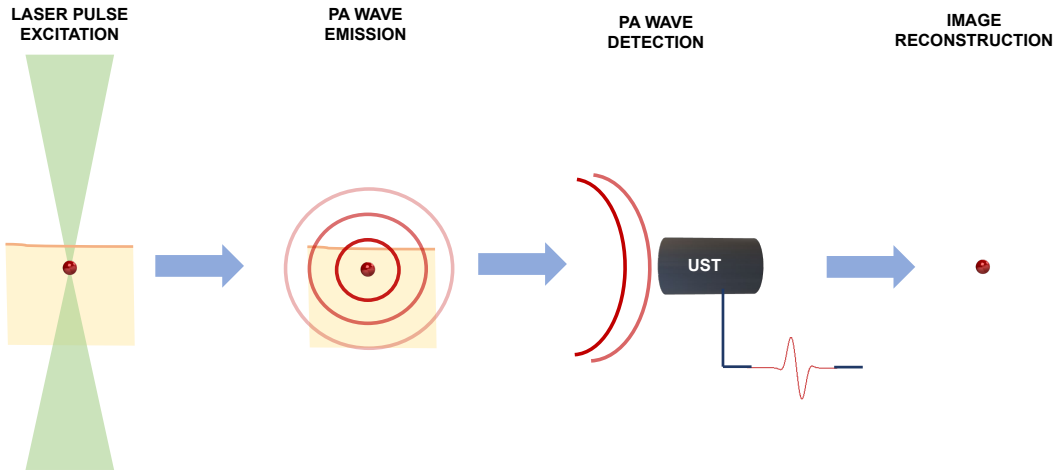

Figure 1.1: Photoacoustic imaging process scheme. UST: Ultrasound transducer.

In PAI, image contrast is offered by absorbance differences between chromophore molecules, which depend on the selected laser radiation wavelength. Hence, this technique allows to select the imaging target by varying the laser source frequency (Xia et al., 2014). The most common endogenous chromophores excited with both visible and near-infrared (NIR) lasers are hemoglobin and melanin, making possible to obtain high-resolution angiographies to monitorize and detect different types of cancer and their time evolution using non-ionizing and non-destructive radiation (Yao & Wang, 2014). Moreover, different exogenous contrast agents with high optical absorption at certain wavelengths such as dyes like Indocyanine green (ICG) or both metallic and organic nanoparticles, have been employed to improve image quality and also for tissue-targeted localization imaging (Yang et al., 2009).

Compared to purely US techniques, PAI allows both molecular and functional imaging of selected biomolecules. Also, it offers a greater penetration depth when compared to pure optical imaging with remarkable resolution due to the ultrasonic detection of the optical excitation (Beard, 2011).

Depending on the PAI modality and the selected components configuration, the system cost, spatial resolution, and image field of view (FOV) variates. Two main branches have been developed over the years, photoacoustic tomography (PAT) and photoacoustic microscopy (PAM). PAT enables larger and deeper volumetric images by illuminating a portion of tissue with diffuse light. Then, reconstruction algorithms are implemented to convert the multiple PA signals received by the ultrasound transducer into spatial information of the irradiated chromophores. Depending on the system application, both laser and ultrasound design can change. For instance, in order to obtain high resolution images of a brain, breast or limbs, the whole imaging sample might be surrounded by custom designed array of detectors increasing the system complexity (Na & Wang, 2021). However, studies for implementing PAT in common handheld US

probes have also been reported, easing its implementation for clinical purposes at a lower cost (Jiang et al., 2022).

On the other hand, PAM aims at obtaining higher resolution images of smaller areas at lower penetration depths, for which lower laser powers are required. PAM allows to image superficial micro-vessels of the skin with very high resolutions at imaging depths up to a few millimeters. Two PAM subcategories exist depending on what establishes the system resolution. In acoustic-resolution microscopy (AR-PAM) a portion of tissue is illuminated with diffuse light, resembling to PAT. The lateral resolution is given by the size of the acoustic focus, determined by the characteristics of the ultrasound transducer. By using high-frequency tightly focused detectors with high numerical aperture (NA), resolutions up to 45 μm have been obtained at a depth of 1.2 mm (Maslov et al., 2005). On the other hand, optical-resolution microscopy (OR-PAM) uses a tightly focused laser beam to generate PA waves, usually detected by a single-element transducer. Hence, the lateral resolution of the system is given by the laser focal spot size, obtaining diffraction-limited resolutions up to less than a micron, with the consequent loss of penetration capability (L. V. Wang, 2008).

Most high-resolution OR-PAM systems are normally based on Q-switched lasers which are able to provide nanosecond laser pulses with a high-quality emission. This eases the system implementation enormously, since they allow to focus the laser beam into very small spots at long distances with negligible energy losses. However, these type of laser sources increase the system cost and worsen the system portability due to their large size. Low-cost laser sources such as pulsed laser diodes (PLDs) or light lmitting diodes (LEDs) have been proposed as an alternative to develop low-cost and portable scanners (Erfanzadeh et al., 2018; Zeng et al., 2013), although their associated low-power and low-quality beams require optical treatment in the form of beam shaping and homogenization (García-Garrigós et al., 2023).

1.2 Motivation and objectives

The use of non-ionizing radiation, the high spatial and temporal resolution and the possibility to use both endogenous and exogenous chromophores as contrast agents have triggered photoacoustic imaging as a powerful tool capable of providing *in-vivo* molecular and functional information, aiding in the early-detection of several types of cancer. It is thus important to continue the research in converting these technologies into affordable and globally-destined systems.

This work is framed in the development of an OR-PAM system prototype. It is based on a previous generation system featuring a laser diode coupled to an optical fiber as a new optical design strategy for improving resolution with low-cost laser sources. Moreover, a US linear array was placed in reflection mode, allowing to obtain competitive resolutions in a clinical-applicable configuration using a low-cost source for the first time (García-Garrigós et al., 2023). However, a poor detection sensitivity along with mechanically scanning the microscope head limited the image quality and substantially increased the acquisition time. The new OR-PAM system will thus include a high-sensitivity focused ultrasound transducer to enhance the image quality, along with a fast laser scanning system that will allow to decrease the image acquisition time.

The present work is centered in the design of an optimum focused transducer, both its geometry and frequency response, that will ensure the image quality improvement. Moreover,

the laser scanning system introduces an issue, since the detection sensitivity worsens outside the focal zone of the transducer. This is also addressed by the implementation of spatial impulse response compensation algorithms, which aim to increase and homogenize the acoustic response along a larger image area.

The main objectives to be achieved in this project are:

1. Obtain the final design of the focused transducer that will be sent to the manufacturer and will be part of the second generation OR-PAM prototype.
2. Implement and evaluate state-of-the-art algorithms to enlarge the sensitivity field of the transducer, and propose if necessary a new algorithm that better suits the requirements of the current project.

Secondary objectives to be achieved in this project are:

1. Assimilate fundamental concepts related to ultrasonic radiation and reception theory
2. Build an OR-PAM simulation environment for testing impulse response compensation algorithms following the prototype design

Chapter 2

Technical background

In this chapter, the main concepts employed for the development of this work regarding photoacoustic excitation, detection and image formation in OR-PAM systems are explained in detail. First, common OR-PAM systems configurations and their main characteristics regarding signal generation using a pulsed laser beam and detection with an ultrasound transducer are described here, along with a review of the current OR-PAM systems performance. Then, fundamentals of spatial impulse response compensation algorithms to enhance the photoacoustic image quality are presented.

2.1 OR-PAM systems configurations

A photoacoustic imaging system can be essentially described as a combination of the signal generation and detection processes. Each PAI modality utilizes different configurations depending on the application and other key parameters as the region of interest (ROI), the desired spatial resolution and frequency bandwidth, among others. This section focuses on the fundamentals of photoacoustic microscopy. A general vision of the excitation-detection process as well as a review of the OR-PAM technology state-of-the-art is presented for a better understanding of the system design problem presented further on.

2.1.1 Photoacoustic signal generation

When employing a pulsed laser with a pulse duration sufficiently short to meet the criteria of thermal confinement (up to hundreds of ns), a rapid temperature increase occurs, leading to a pressure rise due to thermoelastic effects and the subsequent broadband photoacoustic emission when the relaxation takes place (Beard, 2011). The pressure variation generated by the optical energy absorption follows the photoacoustic wave equation (L. V. Wang, 2008), whose pressure distribution can be written as:

$$p_0(r) = \Gamma H(r) \tag{2.1}$$

being Γ the Grüneisen parameter, a tissue-dependent constant that determines the conversion efficiency of the heat deposited by optical absorption into pressure. It depends on thermodynamical parameters of the medium as $\Gamma = \beta c_s^2/C_p$, where β is the thermal expansivity, C_p is the specific heat capacity at a given pressure, and c_s is the speed of sound in the tissue. $H(r)$ refers to the deposited energy density, which equals the product of the absorption coefficient μ_a and the optical laser fluence ϕ, defined as the optical energy per unit of irradiated area. Developing these parameters into Eq. 2.1 (Beard, 2011):

$$p_0(r) = \Gamma \mu_a(r) \phi(r, \mu) \tag{2.2}$$

Note that optical fluence irradiation on human skin is limited by the American National Standards Institute (ANSI) for clinical applications, which establishes the Maximum Permissible Exposure (MPE) depending on the wavelength, the repetition rate and the pulse width of the laser beam excitation for ensuring that no damage is caused to the tissue.

The generation of PA waves, which in OR-PAM takes place at the tight focus of the laser beam, is thus closely related to the properties of the irradiated medium molecules. The photoacoustic effect can be thus exploited for obtaining quantitative information of the tissue by using multi-spectral excitation, yielding to different photoacoustic responses that can be used to obtain functional information of biological processes.

In addition to the dependence of the response on the excitation wavelength, the generated PA signal will also depend on the laser pulse parameters such as the pulse duration and the focal spot size. Only a limited number of studies analyze the variations in the photoacoustic response as a function of these parameters, and they are mostly analytical and focused on a single study case. In general terms, they establish that, given a constant $\mu_a(r)$ and deposited laser fluence $\phi(r, \mu)$, the received signal energy increases as the focal spot size increases (which can be seen as the acoustic source), and it decreases proportionally to the distance at which it is detected due to absorption effects (Araque Caballero, 2013). It has also been reported that the frequency spectra of the detected signal depends on the laser temporal pulse waveform frequency content, which is extremely related to the laser pulse duration (Agano et al., 2018; Brown et al., 2020). There is an analytical expression in the frequency domain (Tabaru et al., 2018) showing that for an equal τ_p, smaller sources increase the higher frequencies of the emission spectra. Regarding the pulse width, as it tends to a delta excitation (a few ns), the high-frequency harmonics increase their amplitude.

This knowledge highlights the relevance of studying each individual case and knowing the generated signal characteristics, since when the ultrasound wave reaches the transducer active area, a good detection will only occur if the frequency content of the PA signal matches the frequency response of the transducer. This process is discussed in the next section.

2.1.2 Photoacoustic signal detection

The detection of ultrasound waves generated by the photoacoustic effect is commonly performed by transducer probes made of piezoelectric materials, which are able to transform the mechanical pressure waves into voltage signals. Photoacoustic signals have a broadband frequency content and low energy as compared to other conventional ultrasound imaging modalities. In consequence, high-sensitivity and broadband transducers are required for having high quality PA images with high resolution and high contrast. Usually, ceramic materials as Lead Zirconate Titanate (PZT) are the common choice for creating piezoelectric sensors. However, their detection bandwidth is limited and their piezoelectric constants makes them best suited for emission (Araque Caballero, 2013). As a solution, piezo-polymers as the polyvinylidene difluoride (PVdF) provide a much broader detection bandwidth with higher sensitivity, mainly because its acoustic impedance is close to that of water and its pressure-voltage conversion efficiency is much higher (Jain et al., 2015), which make these transducers best suited for the reception of ultrasound waves.

Depending on the PAI modality, the required specifications of the transducer change drastically. However, as a general rule of thumb, the system key parameters to consider are the spatial resolution, the imaging or penetration depth and the detection sensitivity (Yao & Wang, 2014).

As previously stated, several sensing elements surrounding the acoustic source are needed in photoacoustic tomography to obtain complete spatial information, hence ultrasound arrays are required to apply tomographic reconstruction algorithms. On the contrary, single-element focused transducers with large active area are commonly employed in PAM imaging systems. In AR-PAM, since the size of the acoustic focus determines the resolution, high-NA high-frequency transducers are selected to provide the smallest possible focus inside a larger illuminated region, requiring a scanning mechanism in order to form a 3D image (Maslov et al., 2005; Song & Wang, 2007). Ultrasound arrays have also been used in AR-PAM to obtain the image via beamforming algorithms applied to the array elements which help reducing artifacts coming from outside the focal zone (Song & Wang, 2007). In OR-PAM, high-sensitivity single-element focused transducers are usually used to ensure a good detection of the high-frequency and low-amplitude signals generated by the tightly-focused laser beams, commonly in a coaxial alignment configuration of both opto-acoustic beams.

Several spatial arrangements have been implemented to obtain OR-PAM images with high lateral resolution. Fig. 2.1 illustrates several commonly used OR-PAM configurations which provide advantages and drawbacks in terms of cost, sensitivity, and applicability to *in-vivo* imaging in clinical situations (Jeon et al., 2019; Yao & Wang, 2014). In the first configuration Fig. 2.1 (a) called transmission mode, the detector is positioned opposite to the excitation on the other side of the sample being examined. It is implemented when high-NA objective lenses are used to focus the laser beam into small spots for improve the resolution, with the disadvantage of decreasing the working distance (WD) to a few micrometers, hindering the penetration of the laser beam. However, sub-wavelength resolutions have been obtained allowing to image single cells, which can be extremely useful for *in-vitro* scenarios (Seeger et al., 2020).

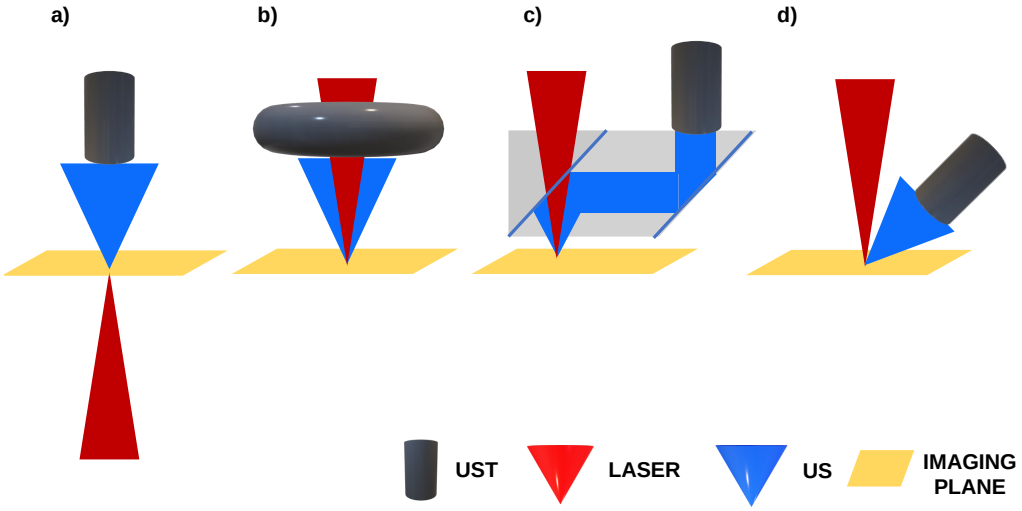

Figure 2.1: Schematic of usable spatial configurations of the laser excitation and the ultrasonic detection in an OR-PAM system: a) transmission mode, b) reflection mode using a ring-shaped transducer, c) reflection mode using a opto-acoustic beam combiner, d) reflection mode using a tilted transducer.

The second one Fig. 2.1 (b), uses a reflection mode arrangement, where a ring-shaped transducer and the laser placed at the same plane relative to the tissue. The detector receives the signal produced by a co-axially aligned optical beam which passes through it. This configuration allows to image living samples, enhancing its applicability in a clinical environment. However, it requires mechanical scanning in order to cover large image areas, since a faster laser scanning can be performed only in the small focal zone of the focused transducer, which is usually less than 200x200 μm. The third option Fig. 2.1 (c), known as beam combiner configuration, encompass an ultrasound reflective surface that totally redirects the acoustic beam to the place where the detector is situated, usually an unfocused transducer with an attached acoustic lens. This system allows to co-axially scan both beams if the reflective surface is a microelectromechanical system (MEMS) scanner, providing fast scanning with high sensitivity. Notwithstanding, high-quality laser beams focused at long working distances are required in order to have enough space to place the combiner, which increases the total system cost. Finally, configuration 4 Fig. 2.1 (d) features a tilted transducer in reflection mode, which can be an unfocused transducer or a linear-array probe, easing the use of a fast laser scanning system with a more affordable mechanism than the beam combiner (2.1 c), although providing low-SNR images.

Different research groups have proposed several configurations depending on the optical beam configuration, the desired imaging target, and other important specifications, that will be reviewed and analyzed in the next section.

2.1.3 Overview of OR-PAM systems

An overview of *state-of-the-art* in the OR-PAM technique is presented here. It is mainly focused, due to the scope of this work, on the transducer selection of each set-up. It is worth noting that there is a trade-off between the key parameters of an OR-PAM system, such as the lateral resolution, the acquisition time, the system applicability to the real clinical practice, the sensitivity of the detection (image quality), and the system cost, which hinders the design of an ideal prototype.

Since the lateral resolution of an OR-PAM system is defined by the size of the laser focal spot, high resolutions are obtained by tightly focusing the laser beam. This is done with high-NA focusing lenses which decrease the laser beam focal or working distance, reaching resolutions of less than a micron in the case of high quality laser beams from Q-switched solid state lasers, limiting its use to *in-vitro* tests in transmission mode. However, remarkable results have been accomplished, having diffraction-limited focal spots of hundreds of nm that allow to clearly distinguish single red blood cells of the order of 7 μm (Dong et al., 2015; Seeger et al., 2020). For OR-PAM systems designed for studying the microvasculature at the capillary level, as well as for imaging skin lesions like melanoma, larger resolutions around 10 μm are usually enough, allowing to work at longer working distances in reflection mode, thus building systems more oriented to clinical practice.

One of the key factors to consider when transferring the technology to the clinical practice is the system cost. In OR-PAM, this is mainly given by using low-cost sources such as PLDs or LEDs instead of high-quality solid-state lasers. However, obtaining competitive and affordable OR-PAM systems is not trivial since this sources provide hardly manipulable laser beams. A few groups have intended to obtain PLD-based systems with a resolution below 20 μm by using objective lenses with high NA, forcing them to work in transmission mode (Erfanzadeh et al., 2018). Only one work has achieved a reflection mode PLD-based system with a lateral resolution of 30 μm, which is the previous OR-PAM system of this work (García-Garrigós et al., 2023). Notwithstanding, several aspects including the acquisition time and image quality still need to be improved in order to obtain a high-quality and low-cost system.

Applicable OR-PAM systems also require low acquisition times. This can be achieved using fast laser scanning mechanisms such as galvanometric mirrors (GM) or MEMS. Unless a beam combiner configuration is implemented (Fig. 2.1 c), the optical beam is scanned rapidly while the acoustic focus remains static. In order to scan larger areas and accelerate the imaging process, usually a large unfocused detector is used in both transmission mode or reflection mode in a non-coaxial configuration, although obtaining low-SNR images due to the sensitivity decrease that these transducers introduce. Studies implementing this set-up obtained a FOV of approximately 6x6 mm^2 in less than 1 minute of acquisition, with a detection sensitivity up to 60 dB less compared to when a focused transducer is used (Xie et al., 2009; Yuan et al., 2012). As a solution, some groups have combined fast laser scanning with great detection sensitivity inside the transducer focal zone, while adding a mechanical raster scanning that moves the microscope head to obtain the whole 3D image, being faster than just a mechanical approach and providing high-SNR images (L. Li et al., 2014). Note that the focal gain in the acoustic focus is proportional to the focusing degree of the transducer. For a high sensitivity detection, high-NA and high-frequency transducers have to be used, which creates extremely tight acoustic

focus, thus limiting the image FOV and the laser scanning range. Another option for avoiding this effect and obtaining a wider FOV is to place a less focused detector, creating a larger focus of approximately 500x500 μm^2, with the disadvantage of decreasing the focal gain (Shi et al., 2011) and thus the SNR of the detected signals.

Regarding the frequency response of the transducer, it should ideally match the frequency content of the generated photoacoustic emission. If high-quality laser pulses with duration of a few nanoseconds are used, the high-frequency content of the generated signal increases. For example, some existing OR-PAM systems use solid-state laser sources that provide 10 ns pulse duration, with a final resolution between 1-10 μm, having a transducer frequency response centered around 40 MHz (Fang et al., 2019; L. Li et al., 2014; Maslov et al., 2005). However, for OR-PAM systems based on low-cost laser sources such as PLDs, where the provided laser pulses duration is usually around 100 ns, the signal spectra shifts towards the lower frequencies, requiring transducers centered around 4 MHz (Erfanzadeh et al., 2018).

In summary, it has been shown how the different components and their configuration can limit the final application of an OR-PAM system. In this work, as mentioned before, a reflection mode PLD-based system is going to be developed using a fast laser scanning mechanism and a high-sensitivity focused transducer. As explained before, some of these concepts influence each other, requiring a compromise in the design to find the optimum components for the prototype. In Chapter 3, the methodology followed to accomplish these objectives is explained in detail.

2.2 Spatial impulse response compensation algorithms

2.2.1 Fundamentals

Considering the transducer properties in photoacoustic imaging (PAI) reconstruction algorithms has been demonstrated key to achieve a superior performance (K. Wang et al., 2010). Characterization of the received signals and their dependence on the spatial and frequency response of the detector can significantly improve both lateral and axial resolution, as well as reduce artifacts (Caballero et al., 2013).

Since the detection and conversion of ultrasonic signals is defined as a linear time-invariant system, spatial and frequency-dependent properties of the transducer can be modeled by its impulse response (IR). A spherical transducer with an infinite reception bandwidth fully surrounding a pressure source located at the center of the sphere has an ideal response, receiving the maximum signal since it detects the entire emitted wave. In a real environment where an ultrasound transducer has a finite size and limited bandwidth, a wave emanating from a source situated at an off-center focus position $r \neq r_0$, where r_0 is the transducer focus position, will arrive at the detector active surface at different times, thus distorting both amplitude and duration of the original pressure signal (Caballero et al., 2013). This can be explained by the Rayleigh's integral, where the transducer active surface S can be divided into a finite number of elements r_s (Jensen, 1999). Hence, the final detected pressure can be considered as the integral of the acoustic fields detected at different points r_s and time instants t at the transducer surface

$$p_{detected}(r,t) = \int_S p(r_s,t)dS \tag{2.3}$$

where the pressure element $p(r_s, t)$ obeys the photoacoustic wave equation (L. V. Wang, 2008), since it is generated by a laser pulse. This process is captured through the spatio-temporal impulse response (SIR), which models the aberrations induced by the detector geometry and the relative position of the source with respect to the transducer focus center. Once the pressure wave, which has a broadband frequency content, has reached the surface of the detector, its piezoelectric properties and the digitalization system after the sensor convert the acoustic wave into a bipolar voltage signal, acting as a band-pass filter around the central frequency of the transducer. This effect is captured via the electrical impulse response (EIR) (Caballero et al., 2013). Then, the combined effect of both system responses is known as the total impulse response (TIR) and is obtained by temporal convolution of both, having:

$$h(r, t) = h_{spatial}(r, t) * h_{electrical}(t) \tag{2.4}$$

where $h(r, t)$ is the TIR, $h_{spatial}(r, t)$ is the SIR, $h_{electrical}(t)$ is the EIR.

Therefore, the detected pressure signal in a real environment can be written in terms of the TIR given by the real transducer configuration as

$$p_{detected}(r, t) = p_{\delta}(r_0, t) * h(r, t) \tag{2.5}$$

being $p_{\delta}(r_0, t)$ the undistorted signal generated by a point pressure source at the transducer focus center (Caballero et al., 2013; Seeger et al., 2020).

Fig. 2.2 shows an schematic of the process of signal generation and detection, for both centered (a) and off-center off-axis (b) sources. The impulse pressure $p_{\delta}(r_0, t)$ is depicted as $x(t)$, $h(r_n, t)$ is the TIR, and $y(r_n, t)$ is the detected pressure signal at each scanning point r_n, which remains almost equal when the source is at the transducer focus and gets distorted as the lateral offset increases.

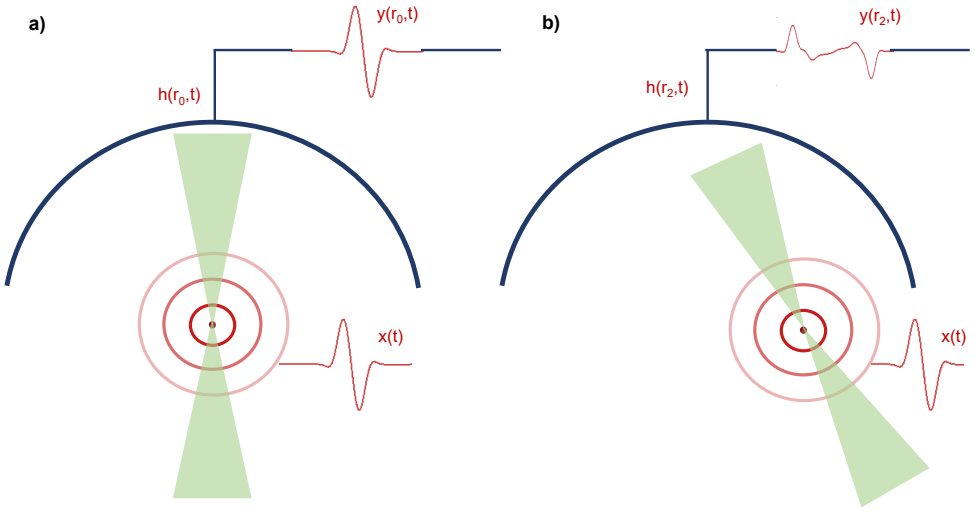

Figure 2.2: Schematic of the photoacoustic signal detection process for a focused transducer in two cases: a) a wave emanating from a centered position r_0, b) a wave emanating from an off-center position r_2. $x(t)$ is the non-deformed input signal coming from a point-like source, $h(r,t)$ are the impulse responses and $y(r,t)$ are the final detected signals after the entire acquisition process. The green beam symbolizes the optical excitation.

2.2.2 Impulse response-based algorithms in PAI

Research groups have developed several approaches for the characterization of the impulse response for different types of transducers. Over the last few decades, the acoustic field calibration of an ultrasound transducer has been performed experimentally via purely acoustical methods operating in emission mode, such as pulse-echo or pressure-field measurement using an hydrophone. This methodology becomes insufficient when translating the matter into the calibration of a transducer with impulse signals working in reception mode only (Q.-B. Lu et al., 2020). As a solution to this issue, the calibration of the transducer spatial and frequency response using photoacoustic sources has been proved very well suited to obtain an input signal similar to an ideal Dirac delta impulse excitation due to their point-like size and short pulse duration from the laser pulsed excitation of a few nanoseconds, which produces a broadband emission spectra wider than the transducer to be characterized (Q.-B. Lu et al., 2020).

Regarding the SIR, several researchers have provided analytical solutions to calculate the spatial response depending on the transducer geometry, easing its calculation without the need for an experimental environment (Jensen, 1999; Lingvall et al., 2003; K. Wang et al., 2010).

With the evolution of numerical calculation environments employed for the development of image reconstruction algorithms as well as different wave propagation research, the SIR calibration has been as well obtained via simulation platforms such as *k-wave* or FIELD II (Chowdhury et al., 2020; Estrada & Razansky, 2019; Jensen, 1997; T. Lu et al., 2020; Treeby & Cox, 2010a; Turner et al., 2014). It has been proven that a synthetic-SIR (sSIR) calibration can be enough for compensating signal aberrations in the image reconstruction process. However, an experimental calibration, at least one at the transducer focus, is needed to take into account the effects of the EIR since this is difficult to simulate, as it depends on the specific transducer piezoelectric

properties and electronics. This yields in a hybrid TIR which is the convolution of the sSIR and the EIR (Caballero et al., 2013). Notwithstanding, in order to record the real transducer response in the 3D imaging space, and to account for the transducer manufacturing imperfections, a proper calibration via scanning a point source though the whole volume is required (Hofmann et al., 2022; Seeger et al., 2020).

In consequence, algorithms including the transducer spatial and electrical properties can be helpful to obtain higher quality images. These have been mainly used in PAT and AR-PAM to reconstruct the signals generated from several absorbers emitting PA waves simultaneously. Hence, model-based algorithms have been able to reduce contributions from sources outside the focal zone, reducing image artifacts, improving the lateral and axial resolution, as well as the SNR (Hofmann et al., 2022; W. Li et al., 2022; T. Lu et al., 2020; Luo et al., 2021; Turner et al., 2014). Moreover, they can account for aberrations induced by the absorption and refraction through different layers of tissue during the propagation until the wave reaches the transducer, which has been proved helpful in transcranial PAI as well as in handheld PAI (Chowdhury et al., 2020; Estrada & Razansky, 2019).

In the case of OR-PAM systems, only a straightforward algorithm is needed to obtain photoacoustic images. At every scan point, the peak value of the pressure amplitude signal generated by the laser focal spot and detected by the transducer is the value of the image pixel, yielding a Maximum Amplitude Projection (MAP) image. However, this techniques can be transferred to a case in which an OR-PAM setup using laser-scanning with a fixed focused single-element transducer is used. In this situation, the amplitude of the distorted signals generated from off-center sources can be compensated, allowing the enlargement of the transducer FOV. In a recent study, the first experimental-TIR algorithm for an OR-PAM was implemented for reducing image aberrations along the axial direction of the laser beam, obtaining undistorted high-SNR and high-axial resolution images (Seeger et al., 2020). For the best of our knowledge, this type of algorithms have not been implemented in OR-PAM for the purpose of enlarging the FOV of the transducer to the millimeter level for allowing to constrained set-ups with low working distances to perform fast laser-scanning with great sensitivity.

Chapter 3

Methodology

In this chapter, the methodology for the development of this work is presented. It is structured in two main parts. In the first one, the ultrasound design process is explained from the initial approach to the optimization and election of the detector. Secondly, a simulation study for the implementation of spatial impulse response compensation algorithms based on the designed transducer is carried out.

3.1 Ultrasound transducer design

In order to obtain the most suitable focused transducer design for the OR-PAM prototype, the main geometrical parameters, such as the curvature radius or focal length, R, and the aperture, a, have to be selected. These parameteres will change the system performance in terms of detection sensitivity and scanning area. The Rayleigh-Sommerfield (R-S) radiation model is employed to characterize the acoustic focus in terms of the emission frequency and the geometrical parameters R and a.

A ring-shaped focused transducer is selected for the PAM imaging system, as a central aperture to allow the optical beam to excite the imaged sample is required (Section 2.1.2). Taking into account the spatial limitations arising from the use of a low-quality laser source and with the aid of the R-S analysis, an analytical optimization process of the transducer geometry is performed to select the best geometrical parameters that will ensure the best possible performance.

Apart from the geometry, the frequency response of the transducer is a crucial factor to consider on the design. It should ideally match the generated PA signal frequency content to ensure the best sensitivity detection. Numerical simulations are carried out to determine the PA signal characteristics from the laser beam parameters, such as the pulse width (τ_p) and the laser spot size. This will guarantee the best design of the sensor for the OR-PAM prototype.

3.1.1 Analysis of the acoustic focus using the Rayleigh-Sommerfield radiation model

The Rayleigh-Sommerfield radiation model provides an analytical expression to determine the radiation pattern of an acoustic source. Here, we consider a spherical focused transducer, as shown in Fig. 3.1. It provides an analytical solution of the acoustic field in every point of the space depending on the selected emission surface. It allows the calculation of the acoustic field generated by complex sources, assuming that their radiation is equivalent to the sum of the radiation of single monopoles distributed over the emission surface (Andrés et al., 2022).

It is worth mentioning that the issue presented herein is to detect broadband photoacoustic waves coming from different points of a 3D image volume, and not to emit single-frequency ultrasound waves. However, this method provides great knowledge about the acoustic focus gain and width in emission mode, which is closely related to the sensitivity decay along the focus in reception mode.

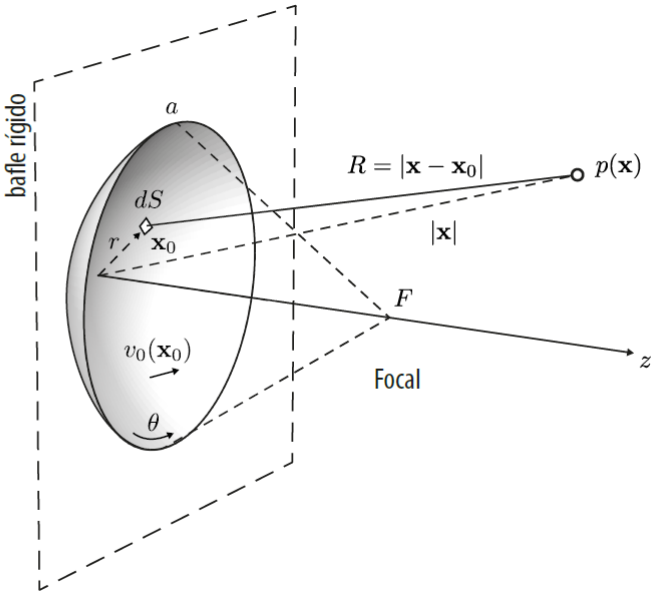

Figure 3.1: Schematic of a spherical focused transducer, where the main spatial and geometrical parameters used in the Rayleigh-Sommerfield radiation model are depicted. Reprinted with permission from (Andrés et al., 2022)

If every point source in the emission surface vibrates uniformly with a velocity $v_0\, e^{i\omega t}$ normal to the surface, the Rayleigh-Sommerfield integral is written as

$$p(x,t) = \frac{i\omega\rho_0 v_0}{2\pi} \int_S \frac{e^{i(\omega t - kR)}}{R} dS \tag{3.1}$$

being x the coordinates of the acoustic field, t is time and $k = \omega/c_0$ the wavenumber. From Eq. 3.1, a numerical solution to determine the acoustic field on a 3D grid can be derived as a sum of the individual sources along the desired emission volume:

$$p(x,\omega) \simeq \frac{i\omega\rho_0 v_0}{2\pi} \sum_{n=1}^{N} \frac{e^{-ik\sqrt{(x-x_n)^2+(y-y_n)^2+(z-z_n)^2}}}{\sqrt{(x-x_n)^2+(y-y_n)^2+(z-z_n)^2}} dS_n \tag{3.2}$$

where $x_n = (x_n, y_n, z_n)$ are the coordinates at each point source at the transducer surface n and $x = (x, y, z)$ are the coordinates of each observation point (Andrés et al., 2022).

For a simple spherical surface like the one shown in Fig. 3.1, acoustic waves converge and the energy is concentrated at the acoustic focus, a small region around the transducer center of curvature. It is characterized by the focus width (W_F) measured along the transversal plane, and the focal pressure increase from the initial value p_0 at the transducer surface, also known as the focus gain G.

From Eq. 3.2, the expressions for W_F and G are derived for a spherical surface in terms of the geometric parameters a and R and the emission wavelength λ, being

$$G = \frac{\pi a^2}{R\lambda} \quad \text{and} \quad W_F = 0.7\frac{R\lambda}{a} \tag{3.3}$$

It can be considered that both parameters are inversely related. As the curvature radius R increases or the aperture a is reduced, a weaker focusing is obtained with lower pressure gain along a wider acoustic focus. An example of this case is shown in Fig. 3.2, where the pressure profile along the axial direction of the acoustic field generated from a spherical surface with $a << R$ using the R-S model can be seen. It is worth noting that they are also dependent of the emission wavelength, having smaller focus with higher acoustic pressure for elevated frequencies.

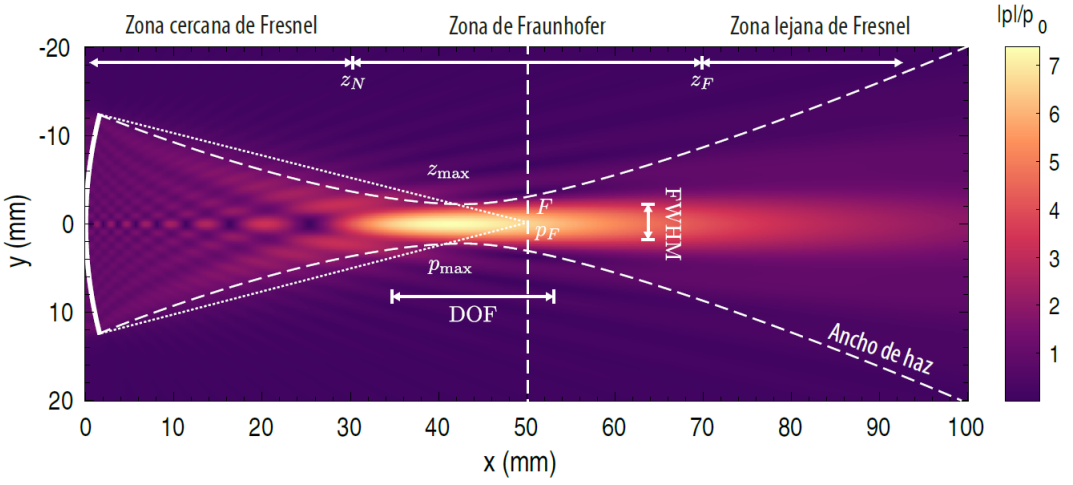

Figure 3.2: Axial view of the pressure field generated by an spherical surface using the Rayleigh-Sommerfield radiation model. Reprinted with permission from (Andrés et al., 2022)

If the spherical surface has a central aperture of a certain diameter as it is the case herein, the expression of G is re-written in terms of the active surface of the transducer S_{active}, which accounts for the loss of sensitivity due to the transducer central aperture (Beissner, 2012), being

$$G = \frac{S_{active}}{R\lambda} \tag{3.4}$$

The equation shows that the focal gain is directly related to the active surface of the transducer, which implicitly depends on the selected a and R values.

Using the expressions above, the W_F and G of four different geometrical configurations are calculated for 1, 3, 5 and 7.5 MHz, as shown in Fig. 3.3. These are emission frequencies chosen to be within the spectrum of the received PA signals for the specific laser beam duration and size. The aperture of the transducer was chosen following the manufacturer specifications of $a \leq 30$ mm and the central aperture was set to 14 mm to place the laser beam optics tube through it as can be seen in the figure (dashed rectangle). It is worth noting that the selected objective lens has a fixed focal length of 10.9 mm, which limits the spatial possibilities that could be carried out. Moreover, to allow the penetration of the laser beam into the patient skin, a distance of 4 mm is set as the margin of space between the edge of the transducer and the center of the sphere. Thus, the microscope head can move as a unit keeping both acoustic and optical focus aligned, allowing to obtain whole 3D scans.

Configuration 1 in Fig. 3.3 is designed to provide the highest possible active area S_{active}, obtained by maximizing the aperture a value and minimizing the shadow region that the optical tube causes. The remaining configurations aim to obtain wider acoustic focus, provided by a lower focusing degree of the transducer. This is achieved by either reducing the transducer aperture a (Fig. 3.3 2,4) or increasing its focal length R (Fig. 3.3 3).

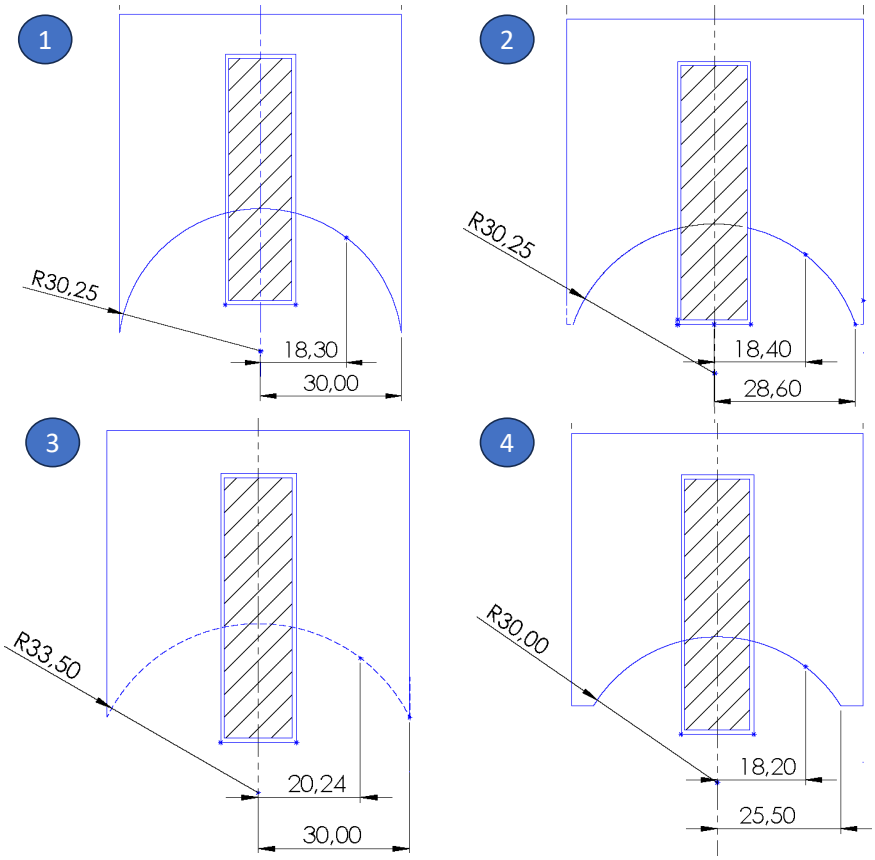

Figure 3.3: Four geometry configurations designed for the R-S model test following manufacturer and the system optics conditions. Small variations of the geometry have been implemented aiming to explore the influence on the focus width and gain.

Although these configurations may help getting an initial transducer design, there are many combinations of a and R that could provide the optimum geometry for a good sensitivity along a wide acoustic focus. In consequence, a deeper analysis is required in order to find out the trade-off between the two design target parameters of gain and focus width, as explained in the next section.

3.1.2 Optimization of the transducer geometry

To solve the trade-off between the inversely-related parameters (W_F and G) that will ensure the best performance of the OR-PAM system, an optimization process has been carried out. The best geometrical configuration will provide a high detection sensitivity along a wide spatial range. The optimization process will be thus defined as a maximization of a product named Gain Focus-width Parameter (GFP), resembling a similar concept in the Electronics field known as Gain Bandwidth Product (Wikipedia contributors, 2023), which is the constant product between an amplifier gain and the bandwidth.

If the expression of the acoustic focus width W_F is written in terms of the *f-number*, a parameter that measures the focusing degree of a transducer, $f_\# = R/2a$, and following the equation of the focus gain for ring-shaped focused transducers, the GFP formula reads as

$$GFP = G\ W_F \simeq \frac{S_{active} f_\#}{R} \tag{3.5}$$

Fig. 3.4 shows an scheme of the optics-transducer spatial configuration, which is limited by the objective lens focal length and the diameter of the tube containing the lens. This will cause a shadow region, decreasing the S_{active} of the transducer.

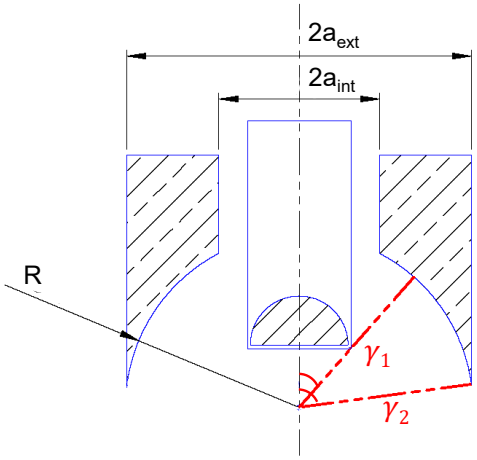

Figure 3.4: Scheme of the ring-shaped focused transducer geometry, indicating the relevant parameters used in the optimization process.

Following the parameters depicted in Fig. 3.4, γ_1 is the angle between the center of the sphere (optical-acoustic confocal point) and the optics tube corner, which remains constant, and γ_2 is

the angle from the center of the sphere to the UST corner, which relates R and a as $a = R\sin\gamma_2$. Note that here a is equivalent to the external aperture a_{ext}.

It is worth mentioning that the GFP parameter does not depend on the emission frequency, which makes it more interesting since it optimizes a purely geometrical relation. The expression of the active surface for a spherical ring-shaped transducer can be written as $S_{active} = 2\pi R^2(\cos\gamma_1 - \cos\gamma_2)$, hence developing Eq. 3.5 the final GFP expression is

$$GFP = 1.4\ \pi\ R\ \frac{\cos\gamma_1 - \cos\gamma_2}{\sin\gamma_2} \tag{3.6}$$

GFP is calculated limiting the problem to the combinations of a and R that could be realistically built, which is limiting the values of γ_2 for each possible R while keeping γ_1 fixed. For this case, $\gamma_1 = 41\ ^\circ$, and $\gamma_1 \leq \gamma_2 \leq \gamma_{2max}$, where $\gamma_{2max} = \arccos(pen/R)$. In the former expression, pen is the penetration depth range of the system, selected to be 4 mm in this case, as explained before. For each value of R, the maximum value of the product is saved, and compared with the rest of maximum values of GFP. The optimum geometry will have the values of a and R that provide the maximum GFP, thus providing the best possible performance of the transducer.

3.1.3 Simulations for the selection of the transducer frequency response

The frequency content of the generated broadband PA signal should match the transducer frequency response in order to ensure the best sensitivity in the detection. The frequency content will vary according to the excitation laser beam parameters, such as the pulse width and the focal spot size. A numerical analysis using the simulation platform *k-wave* (Treeby & Cox, 2010a) has been carried out to obtain the most suitable transducer in terms of its frequency bandwidth.

K-wave is a MATLAB (MathWorks, Massachusetts, USA) toolbox that allows the simulation of impulsive acoustic signals in such a way that the signals generated by the photoacoustic effect can be reproduced. It also allows to simulate the acoustic absorption that takes place as the wave propagates through a medium. *K-wave* is based on the first-order differential equations that govern the mass, momentum and energy conservation inside a medium (Treeby & Cox, 2010b). One of the advantages of this tool is that it works using a pseudo-spectral approach, which means that it resolves the first-order equations in the spatial frequency domain (k-space), allowing it to be computationally faster than other numerical schemes.

There are some main parameters that need to be defined in order to perform a simulation, which are (Pi Martín, 2021):

- The computational grid, the spacing of which limits the maximum spatial frequency that can be measured, complying the Nyquist criteria. Since PAM sources are on the scale of microns due to the tightly focusing of the laser beam, the simulation voxels *ds* have to be small enough to allow the broadband high-frequency signals to propagate correctly though the grid.
- The simulation medium, which is usually considered homogeneous for simplicity. However *k-Wave* allows to use heterogeneous medium for realistic simulations adding some terms to the basic equations.

- The acoustic source, defined as an initial pressure condition that can be defined following a determined function, in this case a rectangular pulse of a few nanoseconds.
- The sensor, defined as a mask within the grid of detector voxels, that records the whole pressure temporal-waveform. In detection approaches like the one in this case, the sensor is defined as a finite number of sensors usually following a certain geometrical shape simulating the ultrasound transducer.

For this study, an homogeneous aqueous medium with a grid spacing ds of 20 μm, with sound speed $c_0 = 1500\ m/s$ and $\rho_0 = 1000\ kg/m^3$ is selected, and the sensor is set as a point-like detector near the source, since the scope of this analysis is the signal properties depending on the source characteristics, and not a realistic reconstruction of the sources. Fig. 3.5 shows a scheme of the used simulation set-up.

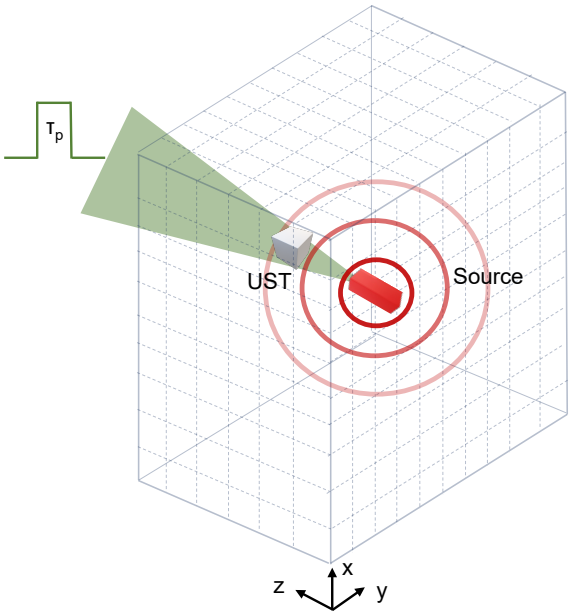

Figure 3.5: Scheme of the *k-wave* simulation environment used for the frequency content analysis, where the acoustic source is defined to have the shape of the laser focal spot, and a point detector near the source detects the generated PA signal. The green region represents the laser beam, whose pulse width is also introduced into the analysis.

Influence of laser focal spot size

A cylindrically-shaped source has been employed to represent the laser spot size, i.e., the portion of tissue generating photoacoustic waves . Variations in the depth of field (L_{DOF}) and width (L_{WF}) of the laser focal spot are introduced, as shown in Fig. 3.6, to understand the effect of the laser spot on the signal characteristics. A 100 ns laser pulse is used for the analysis. Transversal sizes of 10 to 50 μm measured at the Full Width at Half Maximum (FWHM) have been considered for the focal width L_{WF}. The proportion between the focus width and depth is established as $L_{DOF} = 3\ L_{WF}$ to approximately comply with the Rayleigh criteria, where the L_{DOF} is defined as twice the Rayleigh range (García-Garrigós et al., 2023). These values include some of the possible optical configurations that could be used in the prototype, and some other values in between. This analysis is crucial to select the perfect frequency response that could match all the optical configurations.

The influence of the source size variation along the axial plane, L_{DOF}, while keeping the focus width unchanged, is also studied. In this case, $L_{WF} = 10\ \mu m$. The comparison is carried out between a point source ($L_{DOF} = L_{WF}$) and real-shaped sources of ($L_{DOF} = 3\ L_{WF}$ and $L_{DOF} = 5\ L_{WF}$)

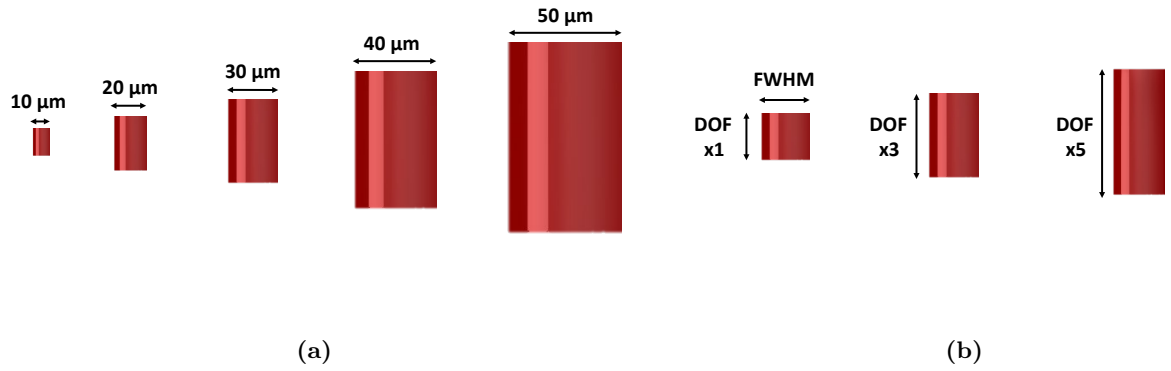

Figure 3.6: The laser focal spot size is introduced as the acoustic source size, and its variations are analyzed for both a) transversal plane (L_{WF}) and b) the axial plane (L_{DOF})

Influence of laser pulse width

Another relevant optical parameter is the influence of the laser temporal profile, or pulse width τ_p. As previously stated, the duration of the excitation has to comply the stress-confinement condition, usually between 1 to 150 ns. This feature can be modeled in *k-Wave*, where the initial pressure p_0 of the acoustic source has a temporal transition that represents the laser excitation. Along with the pulse duration, another parameter to take into account is the rise time of the pulse. Since the laser diode is managed by a pulse driver that creates the ultra-short voltage pulses, an imperfect slower rising edge and a fast falling edge is produced, instead of a typical rectangular pulse. This can create variations in the photoacoustic signal, since the signal frequency content is highly related with the frequency content of the laser pulse.

Selection of the transducer bandwidth

Once the frequency content of the generated signal for a certain source size and laser pulse width is known, the frequency response of the transducer is analyzed. The manufacturer of te¡he transducer provided a datasheet of existing PVdF transducers of their own ("Passive Cavitation Detector Datasheet - Precision Acoustics", n.d.), as shown in Fig. 3.7. The frequency response of the simulated signals can be limited accordingly to determine the energy loss due to the limited bandwidth.

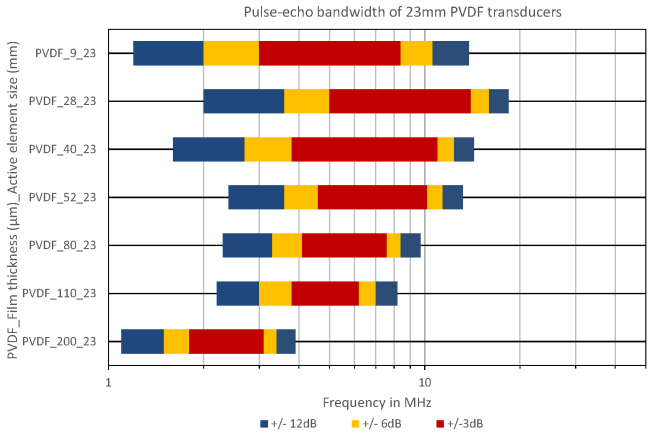

Figure 3.7: Example of some existing PVdF transducers frequency response from the manufacturer. Reprinted from ("Passive Cavitation Detector Datasheet - Precision Acoustics", n.d.)

This process is carried out by filtering the pressure signals with a frequency-domain Gaussian filter simulating a transducer frequency response with a certain central frequency and reception bandwidth. It can be seen as a linear system scheme, where $X(f)$ is the photoacoustic signal spectra, $H_n(f)$ are the n different filters, and $Y_n(f)$ are the output signals, simulating the detected signals in a real-like environment. To quantify this effect, an energy loss ratio is calculated as

$$E_{loss} = 1 - \frac{E_{UST}(f)}{E_{nofilter}(f)} = 1 - \frac{\int A_{UST}(f)df}{\int A_{nofilter}(f)df} \tag{3.7}$$

where $A_{UST}(f)$ is the spectral amplitude of the filtered signal with the applied filter, and $A_{nofilter}(f)$ is the spectral amplitude of the full-bandwidth signal before applying the limited frequency response. This ratio is obtained for some of the shown frequency responses, for sources of different sizes from 10 to 50 μm.

3.2 Evaluation of impulse response compensation algorithms

In the second part of this work, an implementation of some impulse response-based algorithms is carried out. They are based on a previous calibration of the IR, which in this case is performed via *k-Wave* simulations. With this step, the radially decreasing sensitivity field of the selected transducer is known for the entire image region. With the implementation of these algorithms, the limited FOV of the transducer can be enhanced, allowing to perform high-SNR within a larger laser scanning range.

3.2.1 Selected algorithms

For this study, three SIR-based algorithms are analyzed and compared in different situations. These are implemented in a back-projection scheme, which involves low computational cost when compared to model-based iterative algorithms (Hofmann et al., 2022; W. Li et al., 2022). For this reason, the selected algorithms are a suitable solution to resolve the effect of the fast laser scanning with a fixed focused transducer without worsening the computational efficiency (T. Lu et al., 2020; Seeger et al., 2020).

Spatially-variant filtering (SVF)

As shown in Eq. 2.5, once the total impulse response of the system is calibrated, the original undistorted signal $p_\delta(r_0, t)$ can be recovered by the deconvolution of the detected signal at each position $p_{detected}(r, t)$ with the calibrated $h(r, t)$ at the same position r,

$$p_{compensated}(r, t) = p_{detected}(r, t) * h(r, t)^{-1} \simeq p_\delta(r_0, t) \tag{3.8}$$

This is known as spatially-variant filtering (SVF), and it takes place at the signal level. It can be written in terms of the Fourier (spectral) domain to improve the computational efficiency, turning the temporal deconvolution into a division and then obtaining the compensated pressure time-domain signal as

$$P_{compensated}(r, f) = \frac{P_{detected}(r, f)}{H(r, f)} \simeq P_\delta(r_0, f) \tag{3.9}$$

$$p_{compensated}(r, t) = \mathscr{F}^{-1}\{P_{compensated}(r, f)\} \tag{3.10}$$

where $\mathscr{F}^{-1}\{x\}$ symbolizes the inverse fast Fourier transform. This approach provides a fundamental solution for compensating the influence of the detector geometry, computationally efficient (it is a back-projection approach) and without compromising image fidelity (T. Lu et al., 2020). However, if the detection quality is poor, the deconvolution process is extremely noisy in pixels without PA signal due to the instability that the division introduces, even though the signal distortions are correctly compensated in pixels where PA signal is detected.

Spatial matched filter (SMF)

Another algorithm named Spatial Matched Filter (SMF) has been used in the ultrasound imaging environment to overcome spatially-dependent distortions (Jensen & Gori, 2001). It has also been proved as an efficient tool to improve photoacoustic image quality (Gao et al., 2017). In a linear time-invariant system, there exists a filter $SMF(r_n, t)$ that complies

$$p_{compensated}(r_n, t) = p_{detected}(r_n, t) * SMF(r_n, t) \tag{3.11}$$

where $p_{detected}(r_n, t) = SMF(r_n, t_m - t)$ (Jensen & Gori, 2001). Hence, following the convolution properties, the expression can be described as a cross-correlation between the detected pressure signal $p_{detected}(r_n, t)$ and the calibrated non-reversed filter $SMF(r_n, t)$ (Weisstein, n.d.).

Although it derives from the convolution approach explained before, its implementation makes it more robust to noise artifacts. The pixel value of the compensated image is thus the cross-correlation peak value, which is high when the detected signal resembles the calibrated one. Likewise, at a position where there is no absorber and a noise signal is obtained, it will result in an extremely low correlation value. By establishing a threshold, the PA signal is detected and the noise is removed.

Despite being a powerful tool to detect signals even when the raw data is extremely noisy (Gao et al., 2017), if the image is formed with the correlation value it can imply compromising the image fidelity, acting like a segmentation tool instead of just compensating the influence of the transducer. Moreover, this approach implies computing a large number of cross-correlations between the temporal signals of every image pixel and the calibrated model, which can lead to a time-consuming procedure. Note that it is still faster than iterative algorithms based on minimization of a cost function.

Weighted back-projection (WBP)

As a solution to the high computational cost associated to the large 3D dataset like the ones obtained in PAM images, another approach called weighted back-projection (WBP) has been used in impulse response compensation algorithms (Turner et al., 2014). It works at the image level once the Maximum Amplitude Projection (MAP) of the non-compensated image is obtained. It consists on taking the difference between the MAP value of every scan point r of the SIR-calibration signals and the MAP at the focus to build a weight matrix that modifies and compensates pixel-wise the radial amplitude decay. If W is the weight matrix, and I is the PAM 2D image, then the corrected image I' follows:

$$I' = WI \tag{3.12}$$

which provides a fast methodology for compensating the aforementioned effect. Note that if the image has a low SNR, this algorithm will increase the pixel value even though it is a noise pixel, which can lead into a poor image quality.

Algorithm proposal: SVF-SMF combination

Since all the algorithms have benefits and limitations, it has been decided to propose a more robust and reliable algorithm as a combination of two, making use of the efficiency for detecting PA signals from noisy raw data of the SMF, and compensating the amplitude variation using the SVF, since it represents a more fundamental approach and respects the image fidelity.

For low SNR situations, the signals coming from positions with large offsets with respect to the focal point are masked by the detection noise, hence a simple SIR-based SMF approach with thresholding does not work properly for detecting the PA signals. To solve that issue, the deconvolution process (SVF) is performed first, and then a compensated but noisy image is obtained. Then, a SMF filter is applied, based on cross-correlating every compensated non-deformed signal with the original non-deformed PA signal obtained at the focus. With this step, besides improving computational cost (since no 3D model has to be loaded), the correlation is performed in a more effective way having a much higher sensitivity, resembling the case of detecting a PA wave from a noisy signal at the focus or after applying a beamforming algorithm (Gao et al., 2017; Jensen & Gori, 2001). If the correlation value is above a threshold, which is higher and more robust than in the basic SMF approach, the pixel value represents the MAP of the SVF-compensated signal respecting image fidelity.

This proposal is proved with different simulation environments, testing its performance with various phantoms and noise situations. The proposed algorithm workflow for obtaining the definitive MAP value for a pixel with PA source (coloured in green) and for a noise/background pixel (coloured in red):

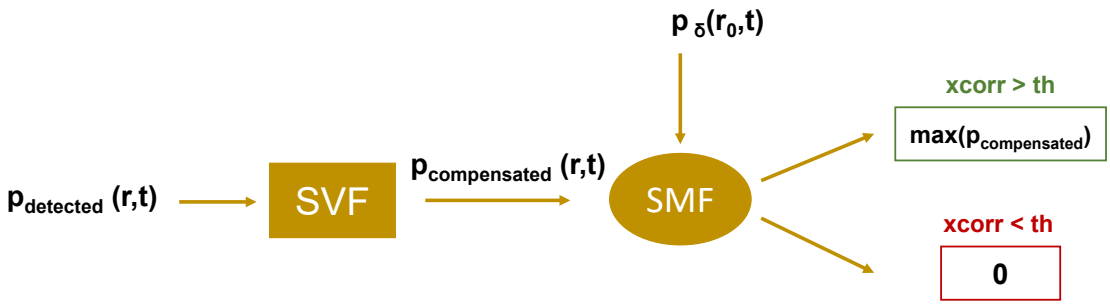

Figure 3.8: Workflow scheme for the proposed algorithm. It shows the process of obtaining the final MAP value for both signal and non-signal pixels. *xcorr* symbolizes the cross-correlation value after the SMF process, and *th* is the established threshold.

3.2.2 Simulations for SIR calibration and implementation of algorithms

A realistic photoacoustic microscopy simulation is performed for the implementation and evaluation of the proposed SIR compensation algorithms. This step introduces variations with the previous simulations presented in Section 3.1.3. A scaled version of the designed transducer is used as sensor to accelerate the simulations while maintaining its geometrical properties. The selected frequency response of the transducer is also modeled. A 20 μm source with a laser pulse of $\tau_p = 100$ ns and a rise time = 20% is used, which are the values that the real prototype will use. Fig. 3.9 shows an scheme of the simulation process for the calibration of the SIR.

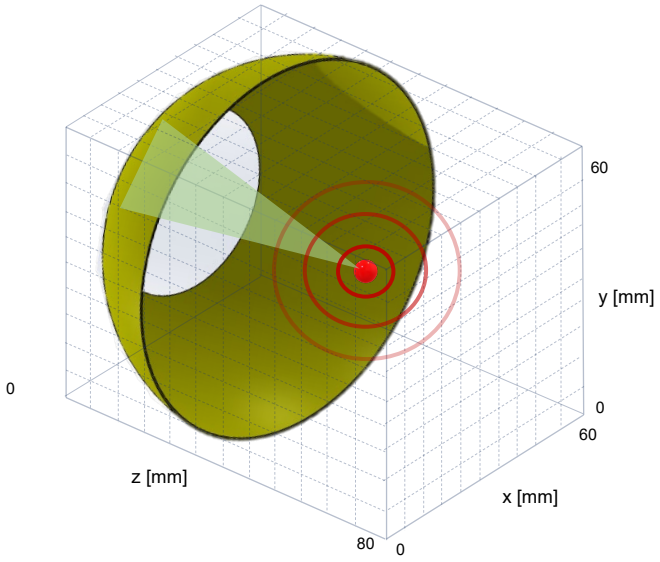

Figure 3.9: Scheme of the $k-wave$ simulation environment used for the SIR calibration, where the previously designed transducer is introduced as the sensor.

This process can be divided in two sub-processes. First, the simulation for the SIR calibration is performed. Once the SIR is calibrated for every scan point, then a second simulation using a vein phantom as an experimental imaging approach is carried out for the implementation of the compensation algorithms.

For the calibration of the SIR, the undistorted signal emitted from the 20 μm point-like source at the center position $x(r_0, t)$ serves as the system input, while the pressure signals detected at every scanning point $y(r_n, t)$ are the system outputs, yielding the impulse response at every position r_n, calculated as

$$h(r_n, t) = \mathscr{F}^{-1}\{H(r_n, f)\} \quad \text{where} \quad H(r_n, f) = \frac{Y(r_n, f)}{X(r_0, f)} \tag{3.13}$$

where $Y(r_n, f)$ and $X(r_0, f)$ are the fast Fourier transform of the time-domain signals $y(r_n, t)$ and $x(r_0, t)$, respectively. Once the scanning simulation is carried out, pressure signals along

the domain are saved in a $SIR_{4D}(x, y, z, t)$ matrix to be used later for the compensation process (Seeger et al., 2020). In this case, only one plane located inside the axial focal zone is simulated for easing the problem, hence the 4D matrix becomes $SIR_{3D}(x, y, z = z_F, t)$. The simulated EIR in this simulations is included since the bandpass filter of the transducer frequency response is acting at every image pixel. Note that this will need to be properly calibrated in an experimental environment to account for real imperfections of the transducer geometry and the digitalization electronics (Caballero et al., 2013; Seeger et al., 2020).

Once the first simulation is completed and the SIR is fully calibrated, a second simulation is carried out mimicking the PAM experimental laser-scanning test using the vein phantom binary mask shown in Fig. 3.10. For this step, a real-shaped 20 μm source with a $\tau_p = 100$ ns laser pulse is used. It is scanned through a 1x1mm area. The obtained outputs are the SIR-deformed pressure signals $p_{real}(r_n, t)$, which are equivalent to convolve the non-deformed signal obtained at the focus $p_{real}(r_0, t)$ with the calibrated spatial impulse responses $h(r_n, t)$ at every point r_n. Note that from now on, $p_{detected}$ is named p_{real} when it is the pressure signal detected from a real-shaped source in a simulation of an experimental environment.

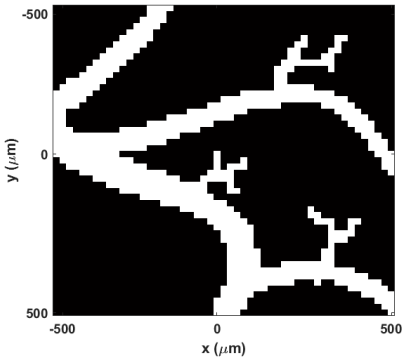

Figure 3.10: Vein phantom used to obtain the PAM images from the algorithms simulations. Note that the phantom is only a transversal plane (top-view) situated at the focus of the transducer axial location $z = z_F$ for simplicity.

Different steps with environments of increasing complexity are followed to obtain a complete overview of their performance. The following scenarios have been considered:

1. Simulation without noise, using an intensity-homogeneous (binary) phantom
2. Simulation with addition of Gaussian noise, having a total image SNR $\simeq$ 20 dB which is not very high SNR compared to other OR-PAM systems, using an intensity-homogeneous phantom
3. Simulation with addition of Gaussian noise of SNR $\simeq$ 20 dB , using an intensity-non-homogeneous phantom, simulating absorbance differences along the veins as an intensity lateral gradient, which can be caused by blood clots, different absorbers concentrations, etc.
4. Simulation with addition of extremely high Gaussian noise of SNR $\simeq$ 10 dB, using an intensity-homogeneous phantom, simulating poor experimental conditions.

Chapter 4

Results

4.1 Ultrasound transducer design

The results of the optimized design of the focused transducer for the OR-PAM prototype are shown next, following the scheme presented in Section 3.1.

4.1.1 Analysis of the acoustic focus using the Rayleigh-Sommerfield radiation model

For the Rayleigh-Sommerfield radiation analysis of the 4 different configurations shown before in Fig. 3.3, the W_F and G values obtained for 1, 3, 5 and 7.5 MHz as emission frequencies are shown in Fig. 4.1a. As the emission frequency increases from 1 to 7.5 MHz, the value of G increases, and the W_F narrows. Regarding the influence of the values of a and R in the analyzed parameters, *Configuration 1* with $a = 30$ mm and $R = 30.25$ mm provides a much larger gain while the focus width value is slightly lower compared to the other analyzed configurations. For this design, Fig. 4.1b depicts the acoustic profile along the transversal plane at the focus ($z = z_F$) for the whole set of frequencies. The effect of the inverse relation between G and W_F is clearly visible.

Following this analysis, the transducer reception bandwidth should be around 3 MHz for having a wide acoustic focus in order to perform large image scans of 500x500 μm while maintaining a high sensitivity . As previously stated, this model constitutes a first approximation, and the acoustic focus created in a broadband reception scenario may differ from the obtained results. Thus, in order to obtain a better solution for the selection of the geometry, the Gain-Focus width Product which is independent of the frequency is used, is presented next.

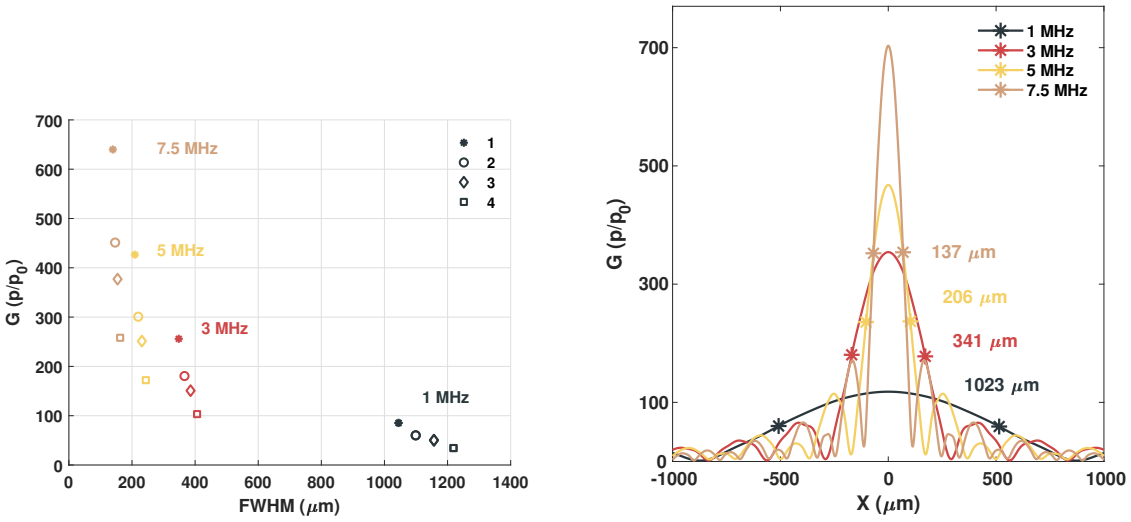

(a) (b)

Figure 4.1: Results obtained from the Rayleigh-Sommerfield radiation model. a) Values of Gain and Focus-width for different emission frequencies of four different geometry configurations. b) Focus lateral profile for *Configuration 1* at different emission frequencies.

4.1.2 Optimization of the transducer geometry

As explained in Section 3.1.2, this step is carried out adding the geometrical limitations for ensuring that the optimum geometry is feasible. The result is shown in Fig. 4.2, where the Gain-Focus width Product value is plotted in terms of the design parameters a and R. The optimization is performed by varying the value of γ_2, hence the optimum aperture a for each value of R that maximizes the GFP product can be known, since $a = R \sin \gamma_2$.

Fig. 4.2 shows that for each value of R from 12 to 45 mm, the optimum aperture a that maximizes the GFP product is always its highest possible value. This is due to the fact that the active surface S_{active} is highly dependent on the selected aperture. Hence, the maximum possible aperture creates the largest surface, which provides the highest focal gain without excessively affecting the focus width.

Based on the obtained results, the optimum geometry that will provide the widest focus width with the higher sensitivity is the one having $R = 30.25$ mm and $a = 30$ mm, *Configuration 1*, examined before in Section 4.1.1. It seems logic since it is the design that provides the maximum S_{active} of all, while the focus width does not drastically decrease compared to the remaining configurations.

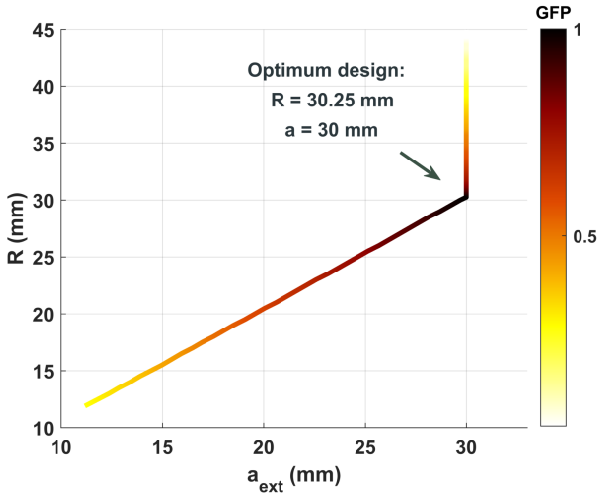

Figure 4.2: Results obtained from the optimization process. The GFP value is shown in a normalized scale for simplicity, and its maximum value, hence the selected geometry configuration, is marked with the black arrow.

Drawings of the definitive geometry sent to the manufacturer for the construction of the transducer after the optimization are shown in Fig. 4.3.

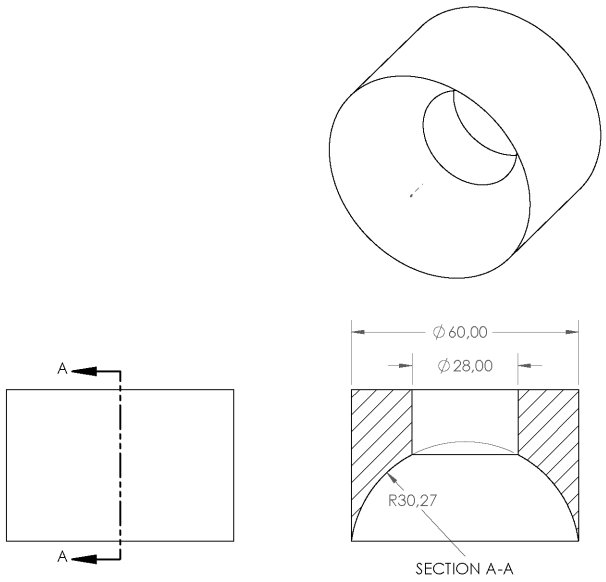

Figure 4.3: Drawings of the final ultrasound transducer sent to the manufacturer for its construction.

4.1.3 Numerical simulations for the selection of the transducer frequency response

The results for the selection of the optimum reception bandwidth of the transducer are shown next.

Influence of laser focal spot size

The portion of tissue excited by the laser spot, which in OR-PAM defines the acoustic source that generates ultrasound waves, affects directly to the characteristics of the PA signal. The influence of the variations in the L_{WF} of the source is shown in Fig. 4.4 (a,b). The temporal waveform (a) for $L_{WF} = 50\ \mu m$ carries more energy, having a smoother transition between the positive and negative peaks as compared to the smaller sources. This is caused by the frequency shift towards the lower frequencies as the source size increases, as shown in Fig. 4.4b, where the normalized amplitude in the frequency domain is shown. It depicts the relative relation between the main lobe and the harmonics, as the absolute differences without normalizing the signals hinders its visualization. For the smallest source analyzed ($L_{WF} = 10\ \mu m$), the main lobe only carries a portion of the signal energy, having high-amplitude harmonics at higher frequencies, while the 50 μm source has the majority of its energy content in the main lobe centered at 5 MHz.

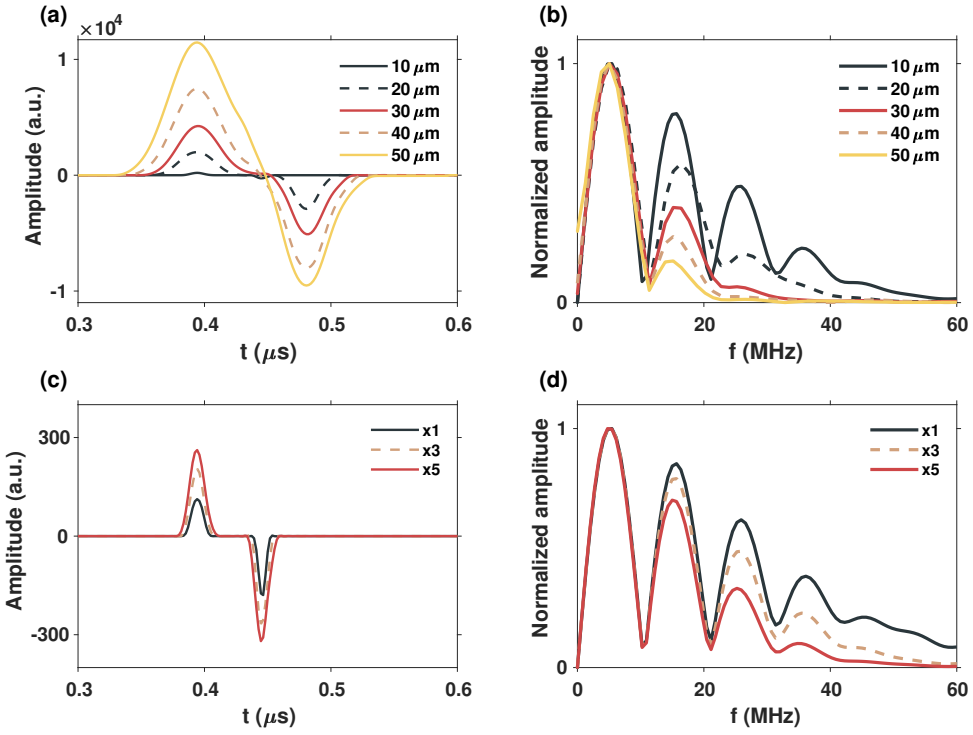

Figure 4.4: Generated PA signal regarding the laser focal spot size. In the upper row (a,b) the variations are introduced in the transversal plane (L_{WF}), while the lower row (c,d) shows the effect of the variations along the axial plane (L_{DOF}) of the source.

The lower row (Fig. 4.4 c,d) shows the influence of varying the ratio between the lateral (L_{WF}) and axial (L_{DOF}) sizes of the laser focal spot. The temporal waveform (Fig. 4.4 c) shows

that the emitted energy increases as the source increase its axial size. However, changes in the spectral content are less noticeable when compared to the effect of the variations along the transversal dimension (upper row). As the source approaches to a point source, the energy of the emitted signal spreads to much higher frequencies.

Influence of laser pulse width

The influence of the laser pulse width in the photoacoustic signal spectra is visible in Fig. 4.5. The effects of the pulse duration τ_p are shown in the upper row. The laser pulses introduced in *k-Wave* as the initial pressure variation are shown in Fig. 4.5 a. For this pulse durations, the normalized spectra of the generated photoacoustic signals is depicted in Fig. 4.5 b. For all the simulations, a laser focal spot of $L_{WF} = 10\ \mu m$ measured at Full Width at Half Maximum ($FWHM$) is used. It can be observed how the photoacoustic conversion is highly dependent on the optical excitation frequency content. For a $\tau_p = 100$ ns, which is the pulse width provided by the PLD driver of this prototype, most of the signal energy is contained in the range from 0-20 MHz, whereas for a $\tau_p = 10$ ns, the main lobe has a bandwidth up to 50 MHz. The lower row plots of Fig. 4.5 show the simulation results of a more realistic laser pulse shape, considering its rise time variation for the case of a 100 ns pulse width. For a theoretical rectangular pulse, the spectral content of the detected signal has more marked harmonics. However, it starts to deform as the pulse rise increases up to a 50 %, where the spectral content of the main lobe remains while the rest become blurred.

These effects match the fact that in most high-quality OR-PAM systems, where the lateral resolution is near 1 μm and the pulse duration is shorter than 10 ns, the emission spectra broadens enormously, thus needing transducers centered between 30 and 50 MHz in order to detect the whole energy. This highlights the relevance of performing simulations for the understanding of the generated signal characteristics, in order to select the best suited transducer bandwidth.

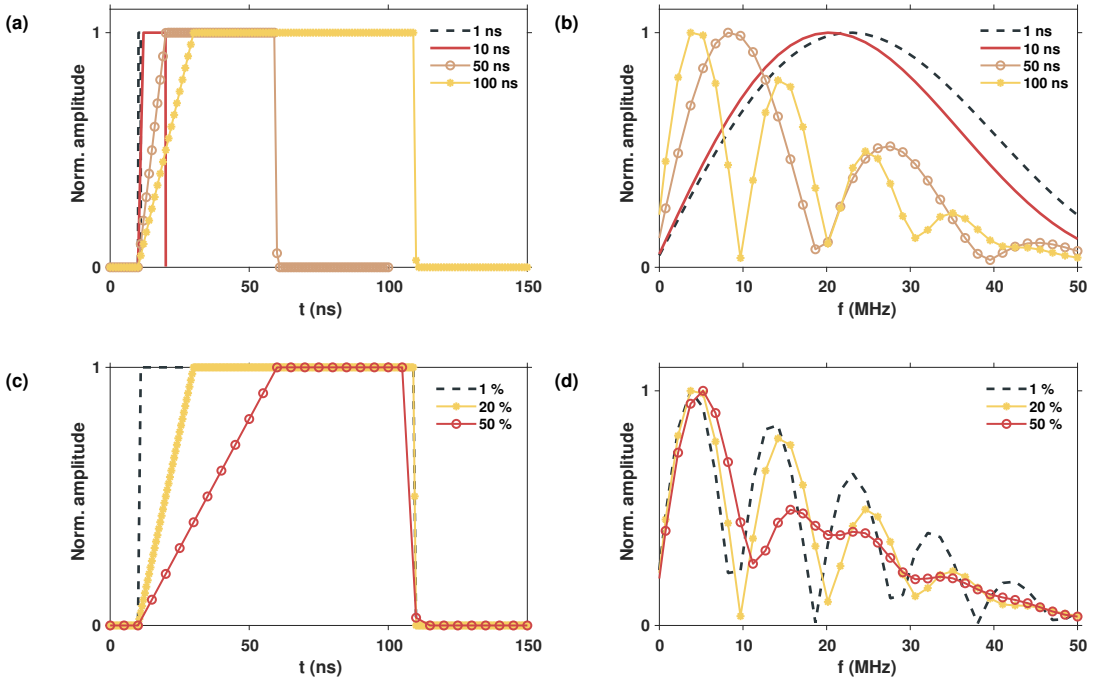

Figure 4.5: Analysis of the influence of the laser pulse width in the generated spectra (upper row), as well as the influence of a more realistic pulse time profile introducing its rise time variation as a proportion of the pulse width value (lower row).

Selection of transducer bandwidth

The available bandwidths provided by the manufacturers (see Fig. 3.7) are introduced in the simulations to analyze the signal energy that is detected compared to the full-bandwidth generated signal, following Eq. 3.7. Results presented in Fig. 4.6 only show the analysis for the first three bandwidths in Fig. 3.7, since these are the widest available, hence the most convenient. The upper row plot is depicted as a linear time-invariant (LTI) system in the frequency domain, where $X(f)$ in (a) is the input which is the unfiltered signal coming from a 10 μm source, (b) shows the three simulated frequency responses $H_n(f)$, and (c) are the filtered output signals $Y_n(f)$ once the $H_n(f)$ have acted on the original signal. The energy loss percentage is calculated as a criterion for the selection of the best transducer bandwidth. Results of this procedure are shown in Fig. 4.6 (d), for source sizes varying from 10 to 50 μm. It can be seen that for the smallest source, 70 % of the emitted energy is lost due to the wider bandwidth that this source generates. On the contrary, for larger sources, the spectra shifts towards the low-frequency main lobe, so that a lower-bandwidth transducer captures most of the signal content (up to a 70 % for the 50 μm source).

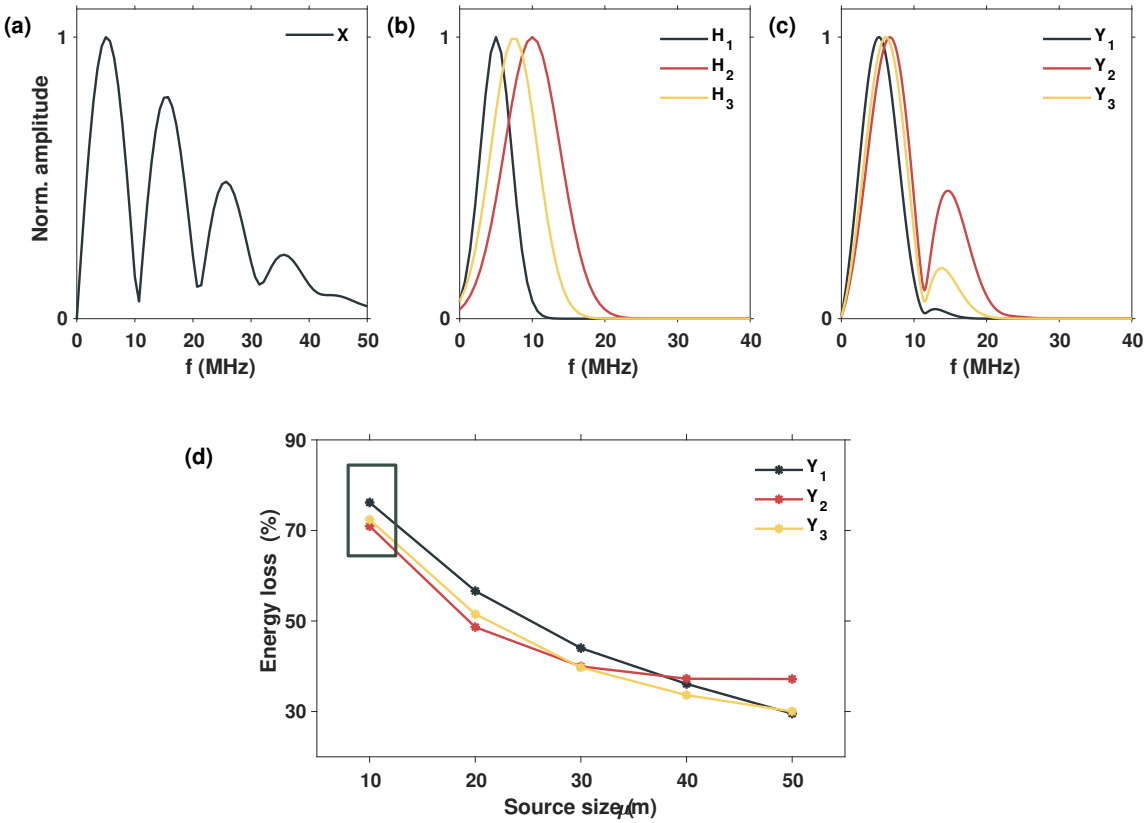

Figure 4.6: Simulations results considering the transducer limited bandwidth as given by manufacturer specs. In the upper row, a) the spectra of the input signal $X(f)$ for a 10 μm source, b) three simulated transducer frequency responses $H_n(f)$, and c) the resulting signals $Y_n(f)$ after the effect of the limited bandwidths. In the lower row, d) the energy loss analysis for laser sources between 10-50 μm. The black box indicates the selection of the 10 μm source which corresponds to the analysis plots of the upper row.

The selected frequency response for the designed transducer is the third one in Fig. 3.7 following the obtained results, also shown as $H_3(f)$ in Fig. 4.6. This will capture as much PA signal energy as possible for all the available laser focal spot sizes, hence ensuring the best detection sensitivity.

Finally, the design of the optimum geometry and the selection of the transducer bandwidth were sent to the manufacturer for fabrication and, afterwards, for the integration in the OR-PAM prototype.

4.2 Evaluation of impulse response compensation algorithms

4.2.1 Calibration of the SIR of the transducer

The implementation of the compensation algorithms is done with the previously calibrated spatial impulse response of the transducer, so it is first obtained via *k-wave* 3D simulations introducing the designed ring-shaped focused transducer. For a 1x1 mm image area, the results from the calibration are shown next in Fig. 4.7, using the MAP representation corresponding to the maximum value of the detected signal at each scanned position of the image plane. It

is shown along with three example of time-domain signals. In this representation, the obtained transducer sensitivity field of approximately 150x150 μm can be seen. Note that this value matches the acoustic focus width obtained with the Rayleigh-Sommerfield model (Section 4.1.1) for an emission frequency of 7.5 MHz, which is the simulated central frequency of the transducer.

The detected signals are distorted in both shape and amplitude as the source separates from the acoustic focus. The signal distortion of the PA wave coming from an off-center position due to the spatial averaging of the spherical wave is summed to the effect of the wave portion loss, which causes a degradation of the detected amplitude. When the source is centered at the transducer focal zone (Fig. 4.7 (i)), the typical N-shaped photoacoustic signal is detected. A 200 μm offset source generates a time-expanded version with an amplitude decrease factor of 6 (Fig. 4.7 (ii)). This effect is more pronounced when the source is at a larger lateral offset of 400 μm (Fig. 4.7 (iii)).

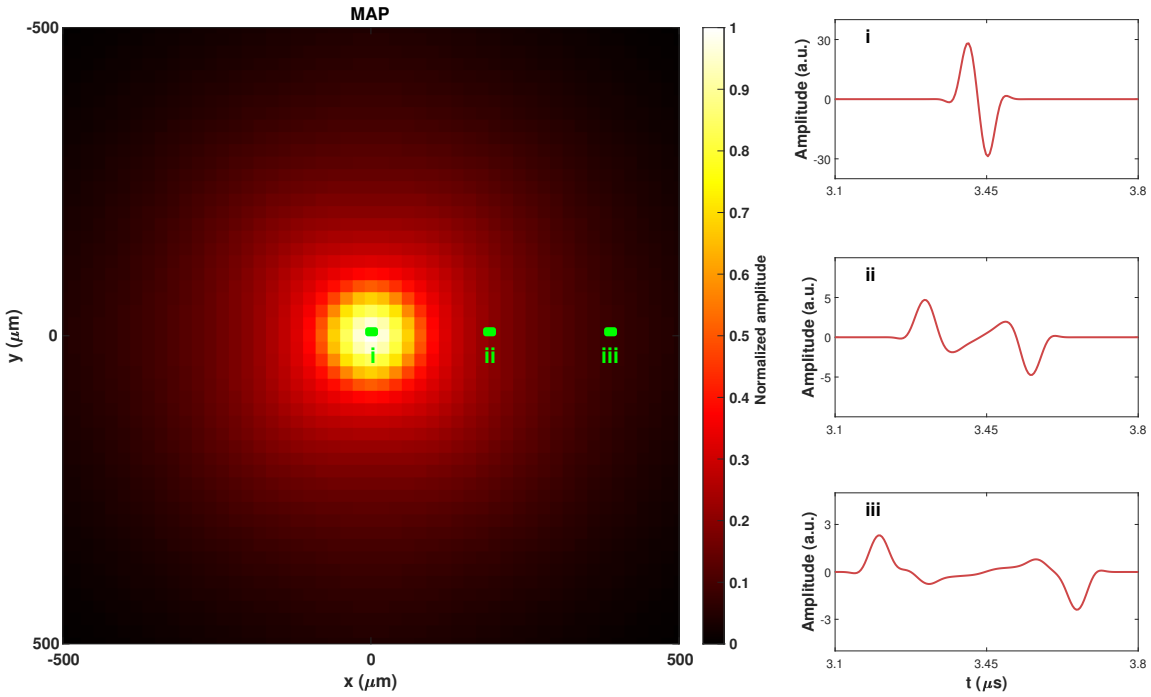

Figure 4.7: MAP image of the sensitivity field of the selected transducer from the SIR calibration simulation. On the right hand side, the detected time signals from i) a centered position, ii) a 200 μm offset position and iii) a 400 μm offset position are represented.

Once all the signals of the 3D SIR are obtained at every point $r_n(x, y)$, their impulse response $h(r_n, t)$ is calculated with Eq. 3.13. Fig. 4.8 shows the followed steps in a visual manner. In the upper row the calculation process for a signal coming from a centered position r_0 is depicted . Fig. 4.8 (a,b) shows both the originally emitted and the detected signals, $x(r_0, t)$ and $y(r_0, t)$, in temporal and frequency domains, respectively. The result from the deconvolution process, and the inverse FFT for obtaining the time-domain response, is shown in Fig. 4.8 (c,d). Note that the detected signal at the focus $y(r_0, t)$ suffers from a barely noticeable distortion, and it is only influenced by the attenuation corresponding to the propagation distance from the focus center to the transducer surface. Hence, the impulse response resembles a bandwidth-limited Dirac delta. This process is also depicted in the lower row for a source located at a position r_1

with a lateral offset of 500 μm. It is visible how the distortion caused by the reception of an off-center wavefront modifies the frequency content, and how this distortion is captured by the impulse response $h(r_1, t)$.

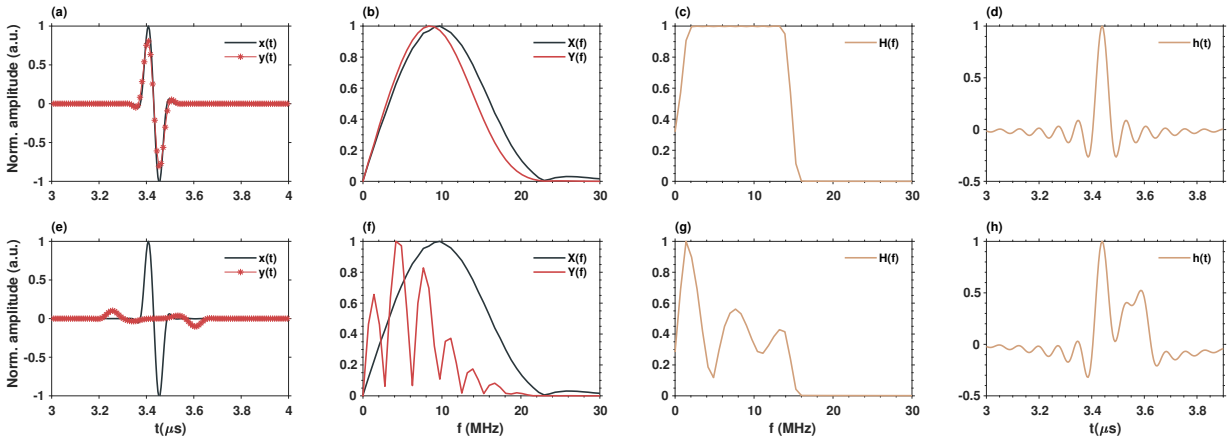

Figure 4.8: Process of calculation (steps from left to right) of the impulse response $h(r, t)$ for a centered position (upper row), and for an off-center position (lower row)

Fig. 4.9 shows all the calibrated impulse responses $h(r_n, t)$ for successive further positions from the transducer focus center. It is visible how the amplitude and shape of the impulse responses are modified similarly to the distortion of detected time signals as the lateral offset increases.

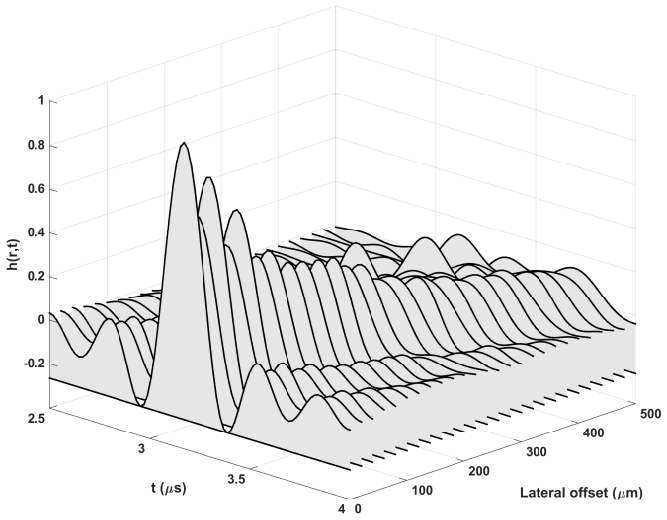

Figure 4.9: Normalized calibrated impulse responses for a lateral offset sweep from 0 to 500 μm.

4.2.2 Evaluation of algorithms: ideal simulations without noise

The results from the implementation of the selected algorithms for a vein image phantom are shown next. First simulations were implemented without addition of noise, to test the algorithms performance in an ideal case.

Spatially-variant filtering (SVF)

The calibrated spatially-variant impulse response $h(r_n, t)$ is the filter which deconvolves the detected signal $p_{real}(r_n, t)$ for every scan point r_n. The obtained MAP images of the vein phantom before and after the SVF implementation are shown in Fig. 4.10 (a,b). It is clearly visible how for a intensity homogeneous vein phantom, the effect of the focusing and the sensitivity radial decay is fully compensated. In Fig. 4.10 (c,d), the time signals corresponding to the detected p_{real} and compensated p_{comp} signals for representative scan positions (i, ii) are shown. In the inlays, the used filters h are depicted. This algorithm shows how deconvolving the calibrated impulse response to the low-amplitude distorted signal p_{real} provides a compensated signal equal to the non-deformed wave captured at the transducer focus.

It is worth noting that this algorithm implies a very low computational cost, since it is performed in the frequency domain.

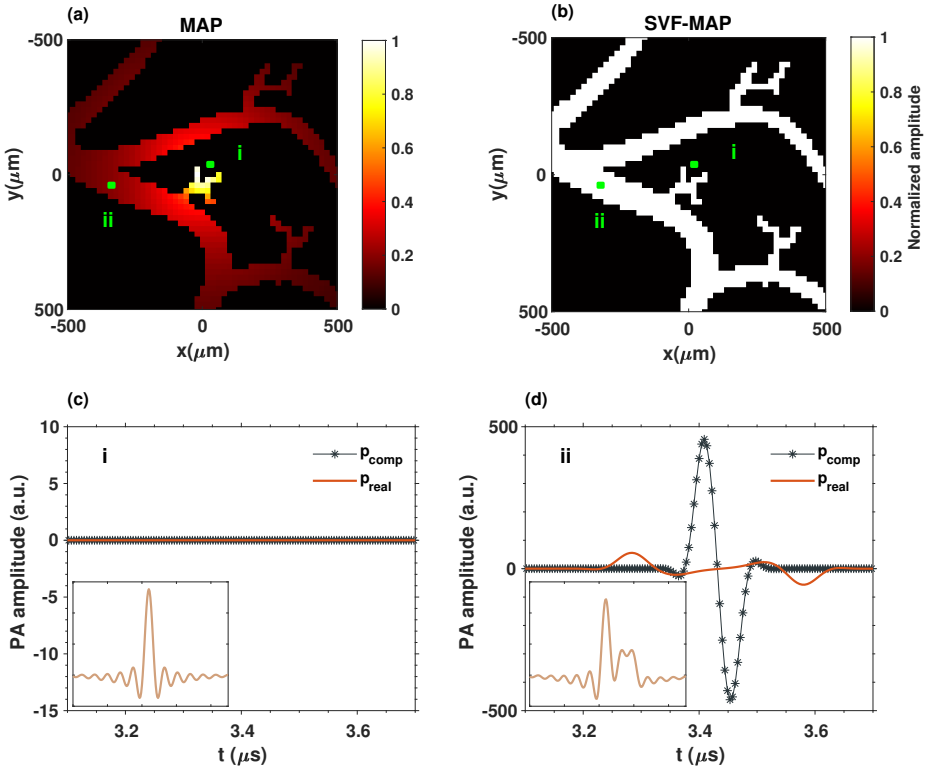

Figure 4.10: MAP images of the a) non-compensated image, b) compensated image using the Spatially-variant Filter in a noiseless environment. The lower row shows two examples of the detected and compensated signals for c) a centered position, and d) an off-centered position. The inlay shows the calibrated impulse response for each of the positions.

Spatial matched filter (SMF)

Fig. 4.11 shows how the SMF algorithm perfectly identifies when a photoacoustic signal is detected, since the time signal of the calibrated SIR at the evaluated position p_{calib} follows a very similar pattern, hence providing fully compensated images in a range of 1x1 mm^2. As explained in Section 3.2.1, when a PA signal is detected, the cross-correlation value will be high even if for a weak signal. This case is depicted in Fig. 4.11 (d), where the correlation value shown in the inlay is maximum. Conversely, for a position where no PA signal is detected (Fig. 4.11 (i)), the cross-correlation value is null.

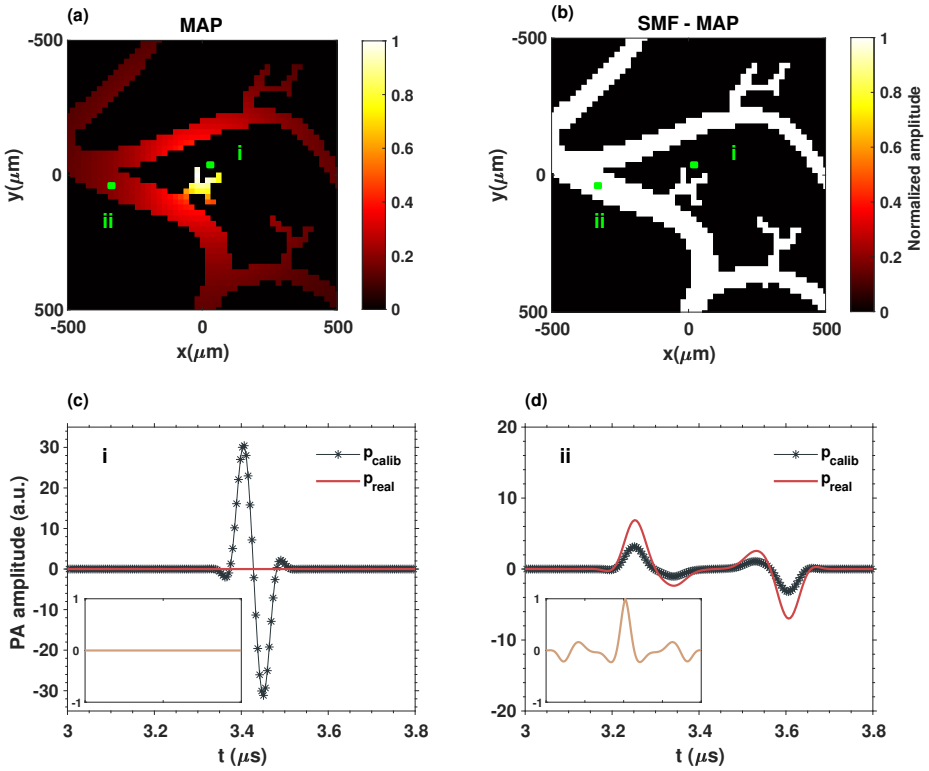

Figure 4.11: MAP images a) without compensation, b) compensation using the Spatial Matched Filter in a noiseless environment. The lower row shows two examples of the detected and compensated signals for c) a centered position, and d) an off-centered position. The inlay shows the cross-correlation output.

Weighted back-projection (WBP)

The evaluation results of this algorithm are shown in Fig. 4.12. The original image I is represented in (I), the calibrated SIR and the weight matrix W which multiplies the original image in (II) and (III) respectively, and the compensated image I' in (IV). At further positions where I and I' have opposite values in the range between 0 and 1, the compensation tends to be non-homogeneous.

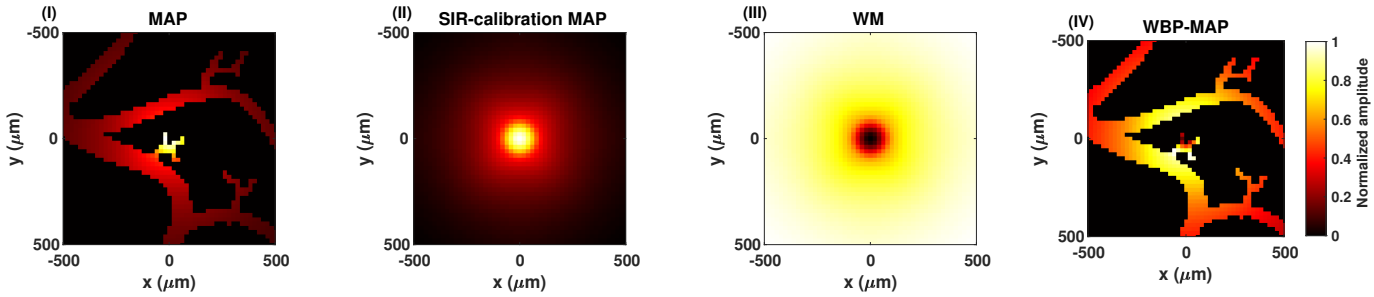

Figure 4.12: MAP images of the i) non-compensated image, ii) SIR calibration image, iii) the used weight matrix from the SIR calibration, and iv) compensated image using the Weighted Back-Projection in a noiseless environment.

Algorithm comparison

To obtain a complete vision of the performance of the three evaluated algorithms, the logarithmic scale representation of the results are shown in Fig. 4.13. It is clearly visible that the SVF and SMF algorithms lead to a fully compensated image, retrieving the original binary mask of the phantom. On the other hand, the WBP provides an amplitude inhomogeneity of 5 dB, leading to a non-uniform compensation.

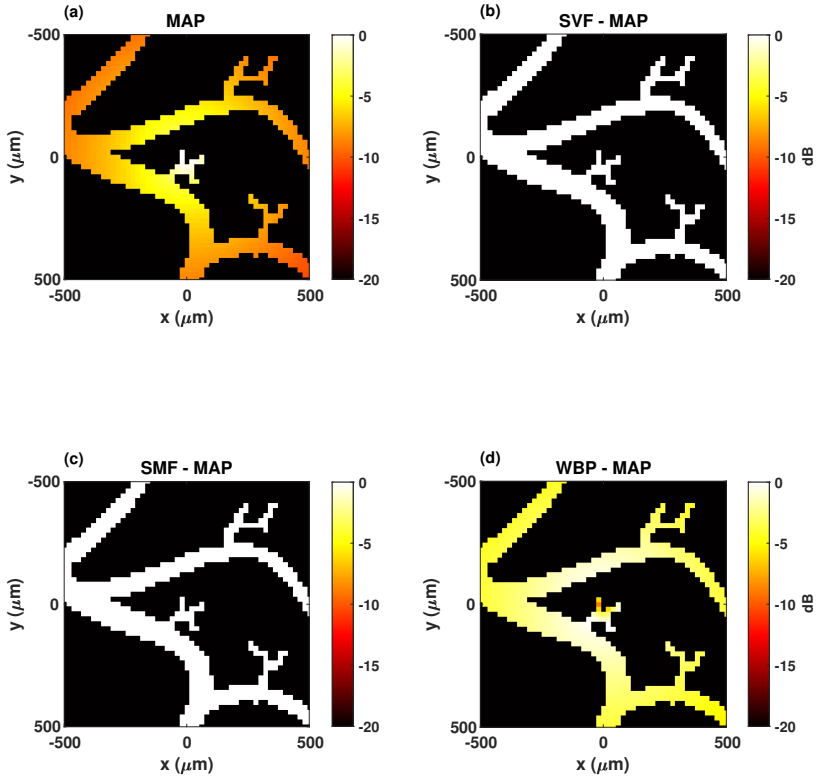

Figure 4.13: MAP images in logarithmic scale (dB) of the a) non-compensated image, b) compensated image using the Spatially-variant Filter, c) the Spatial Matched Filter, and d) the Weighted Back-Projection in a noiseless environment.

Although these results may suggest the best performance for the SVF and SMF algorithms, recovering completely the binary phantom image, a more realistic situation is needed to test their true performance with the addition of signal noise, as it is described further on.

4.2.3 Evaluation of algorithms: addition of noise

In this section, the results obtained with the addition of Gaussian noise leading to a PAM image of SNR $\simeq$ 20 dB are shown. This high noise level was chosen from the average SNR of a previously developed experimental system based on a linear array transducer which had a very low sensitivity (García-Garrigós et al., 2023).

Spatially-variant filtering (SVF)

As previously stated, the deconvolution process involves a non-stable solution due to the division that diverges at pixels where there is only noise, as it shown in Fig. 4.14. Note that for pixels where there is PA signal, the compensation of the sensitivity decay is correctly performed. However, noise pixels levels diverge strongly for the compensated signal worsening the overall SNR, resulting from the division of the noise by the calibrated impulse response.

It is worth mentioning that the calibrated impulse responses (inlays in Fig. 4.14 (c,d)) resemble the ideal situation without noise, which can explain why the compensation in pixels of PA signal works very well. However, the lack of robustness makes this approach insufficient for realistic noisy environments.

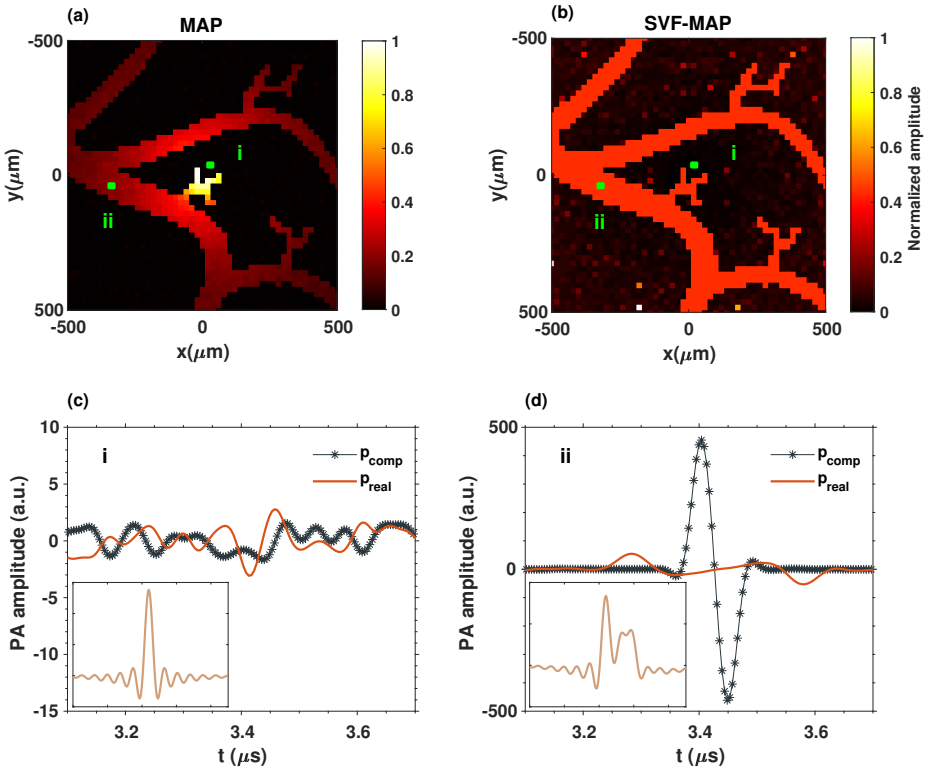

Figure 4.14: MAP images with addition of Gaussian noise a) without compensation, b) compensation using the Spatially-variant Filter. The lower row shows two examples of the detected and compensated signals for c) a centered position, and d) an off-centered position. The inlay shows the calibrated impulse response for each of the positions.

Spatial matched filter (SMF)

Fig. 4.15 shows how the SMF improves the SNR along pixels with absorbers and homogenizes the image. However, it decreases the overall SNR in the noisy pixels, because a pixel value different from zero is assigned unlike in the ideal case without noise.

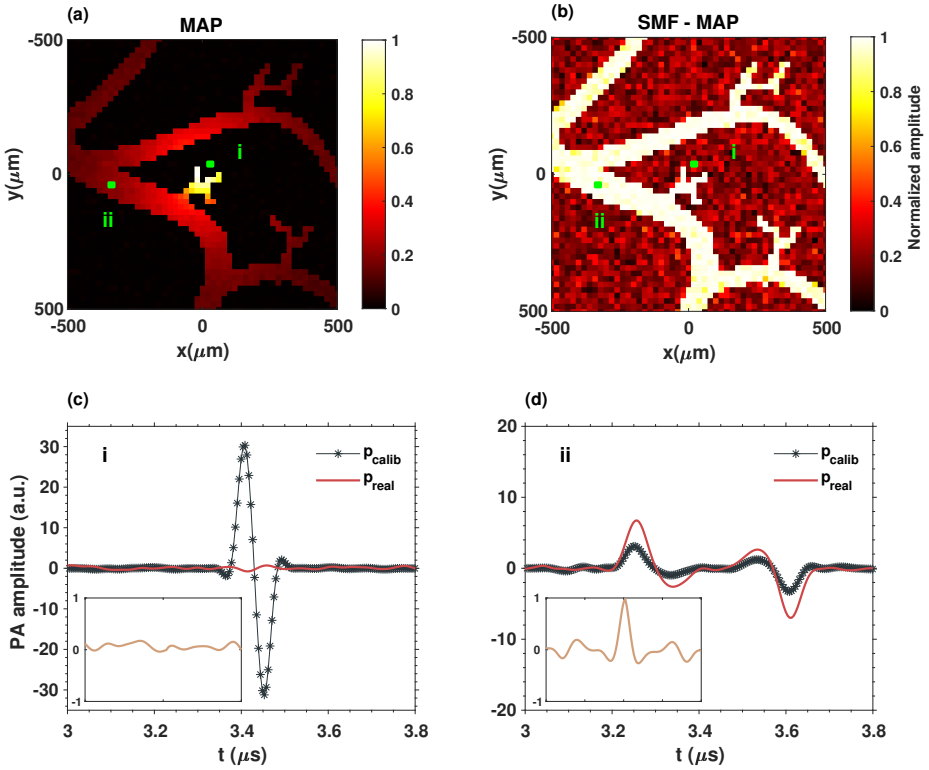

Figure 4.15: MAP images with addition of Gaussian noise a) without compensation, b) compensation using the Spatial Matched Filter. The lower row shows two examples of the detected and compensated signals for c) a centered position, and d) an off-centered position. The inlay shows the cross-correlation output.

Since the noise level is much lower than the signal level, it can be easily removed by thresholding, which cannot be done for the SVF algorithm. The result of this process is shown next in Fig. 4.16, where a threshold of 0.9 is enough for keeping the pixels with PA signal and remove the image background.

This results suggest that, as commented in Section 2.2, the SMF algorithm is an efficient approach for solving the issue posed here, leading to compensated images for 1x1 mm^2 with homogeneous and improved SNR.

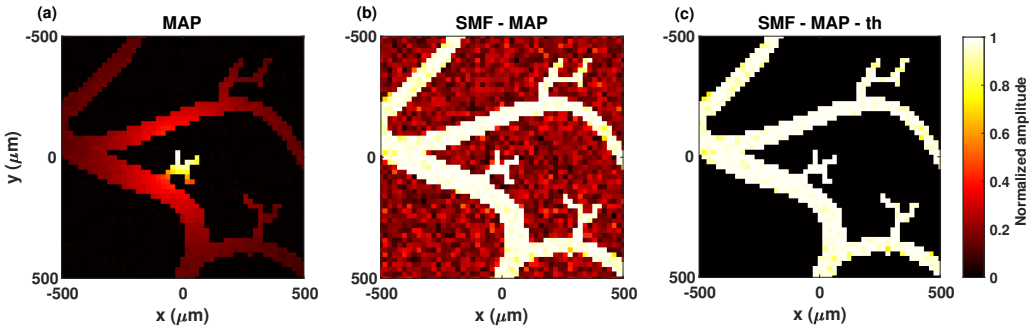

Figure 4.16: MAP images of the with addition of Gaussian noise a) without compensation, b) compensation using the Spatial Matched Filter and c) compensation using the Spatial Matched Filter with the use of a threshold filter of 0.9 in normalized units.

Weighted back-projection (WBP)

Finally, the WBP results showed in Fig. 4.17 depict how in a noisy environment, it does not provide a good performance, since it enhances the noise level radially along with the signal level, and neither compensates the signal correctly. This approach has the advantage of its simplicity, although it lacks robustness when applied to a real scenario with noise.

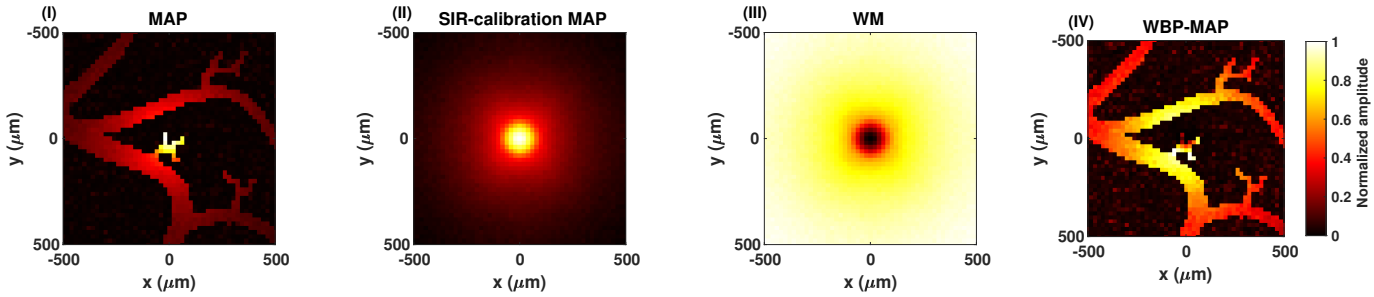

Figure 4.17: MAP images with addition of Gaussian noise I) without compensation, II) SIR calibration, III) weight matrix from the SIR calibration, and IV) compensation using the Weighted Back-Projection.

Algorithm comparison: uniform phantom

A comparison in logarithmic scale between algorithms is also performed in order to have a more grounded conclusion. This comparison is shown next in Fig. 4.18. It can be seen how the SVF homogenizes the SNR along the absorber pixels, although also increasing the noise level, which provides a final average SNR of about 6 dB, compared to the original non-compensated SNR of 15 dB. Regarding the SMF with the thresholding approach, the compensation and SNR enhancement is perfectly carried out for an homogeneous, or binary, vein phantom. For the WBP, as in the linear scale image, the SNR is worsened at least 5 dB and the compensation is not completely accomplished for PA signal pixels.

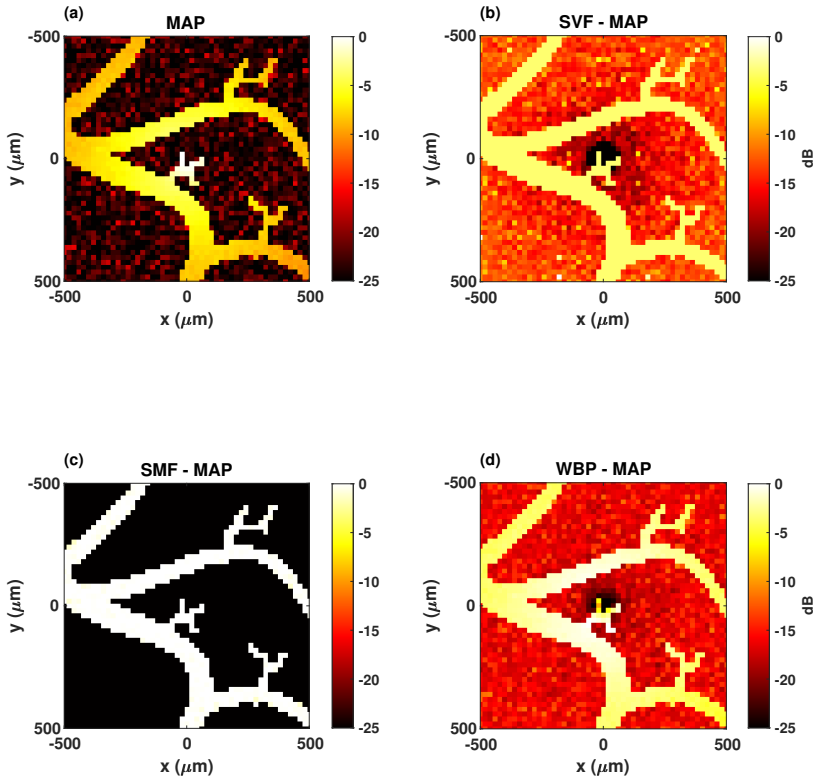

Figure 4.18: MAP images with addition of Gaussian noise in logarithmic scale (dB) a) without compensation, b) compensation using the Spatially-variant Filter, c) compensation using the Spatial Matched Filter, and d) compensation using the Weighted Back-Projection.

Algorithm comparison: non-uniform phantom

In this section, an intensity variation along the lateral direction is introduced in the vein phantom to test the performance of the selected algorithms in a more realistic environment. This simulates a non-uniform intensity response in order to account for absorbance differences in the tissue due to different absorber concentrations or a vein deformity, inducing PA signal intensity variations. With the intensity uniformity (Section 4.2.3), the SMF clearly compensates and binarizes the resulting image, but it has to be proved if the binarization is also obtained even if the phantom is not a binary mask, which could introduce lack of fidelity.

The obtained results are shown in Fig. 4.19, where it is visible that the original distorted image (Fig. 4.19 a) mixes both influences. As suspected, the SMF provides a quasi binary mask and does not recover the intensity variation introduced as a lateral gradient. Moreover, since the signal level on the right side of the image is extremely low, the correlation value is also very low and the PA signal information is removed by the threshold level.

On the other hand, the SVF fully compensates the sensitivity decay produced by the transducer geometry while respecting the intensity levels, although yielding to a PA image with a poor average SNR. Regarding the WPB algorithm, it does not provide a good performance like in the previous simulation environments.

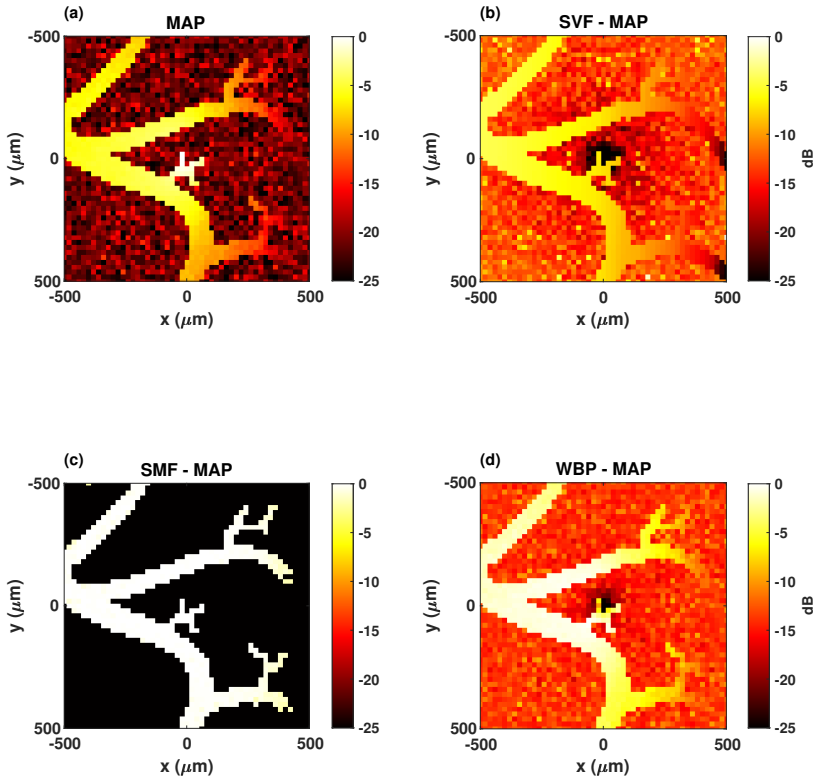

Figure 4.19: MAP images with addition of Gaussian noise in logarithmic scale (dB) for a non-uniform phantom a) without compensation, b) compensation using the Spatially-variant Filter, c) compensation using the Spatial Matched Filter, and d) compensation using the Weighted Back-Projection.

Through this analysis, it becomes apparent that the algorithm initially considered as the most suitable for addressing this issue does not adequately account for variations in intensity levels, thereby impacting the fidelity of the image. Notwithstanding, it is a robust way for detecting PA signals and for noise removal even with an extremely unfavorable situation with 20 dB SNR, as shown before. Hence, an algorithm that combines the detection of PA signals (SMF) and the compensation with intensity level preservation of the SVF could be implemented as a robust-efficient approach as shown in the following simulations combining both algorithms conveniently.

4.2.4 Proposed algorithm: SVF-SMF-Combination

As the final part of this work, the proposed algorithm explained in Section 3.2.1 is implemented in order to solve the aforementioned issues after the evaluation of the individual algorithms. First, in a highly noised image, and then, in a noisy image with a non-uniform phantom.

The results of this approach in a very noisy environment are shown in Fig. 4.20, for the original image with a SNR of 10 dB (a), the obtained compensated but extremely noisy image (b), and the final compensated and clean image after the proposed algorithm (c). The order in which the individual algorithms are applied affects the final image result, since the quality is enhanced and reinforced with this approach compared to algorithms applied in reverse order. For an off-centered position with PA signal, the classic SMF algorithm performs a cross-correlation between two weak signals $p_{real}(r_n, t)$ and $p_{calib}(r_n, t)$ masked by the noise, which yields in a low

correlation value. With this new approach, after the compensation provided by the SVF, the cross-correlation between the corrected signal $p_{comp}(r_n, t)$ and the non-deformed signal model $x_{real}(r_0, t)$ has a higher amplitude compared to the noise, providing a robust and high correlation value. Likewise, the correlation between the undistorted model and the unstable compensated signal of a position without PA signal is extremely low, similar to the ideal case without noise.

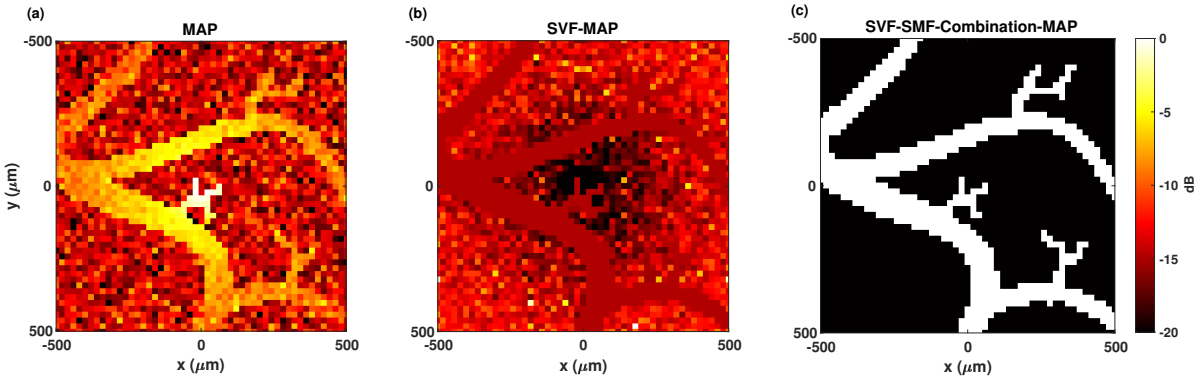

Figure 4.20: MAP images in a extremely noisy environment with an average SNR of 10 dB a) without compensation, b) compensation using the Spatially-Variant Filter, and c) compensation using the SVF-SMF combination algorithm.

Fig. 4.21 shows a workflow schematic with the followed steps for the combination of the SVF and the SMF algorithms, to obtain the final fully compensated image from the original non-compensated. After the application of the SVF, if a PA signal is detected, the compensation is correctly performed. This can be seen following the flow for the pixel labeled as *a*. When the SMF is applied between this compensated signal and the model, which is the undistorted signal at the acoustic focus $x_{real}(r_0, t)$, the cross-correlation value is almost one. For a noise pixel, where the divergence of the deconvolution process (SVF) provides a high-amplitude noise signal, the result of the SMF is a cross-correlation near to zero, hence easily removable by thresholding. This can be seen following the path for the pixel labeled as *b* in Fig. 4.21.

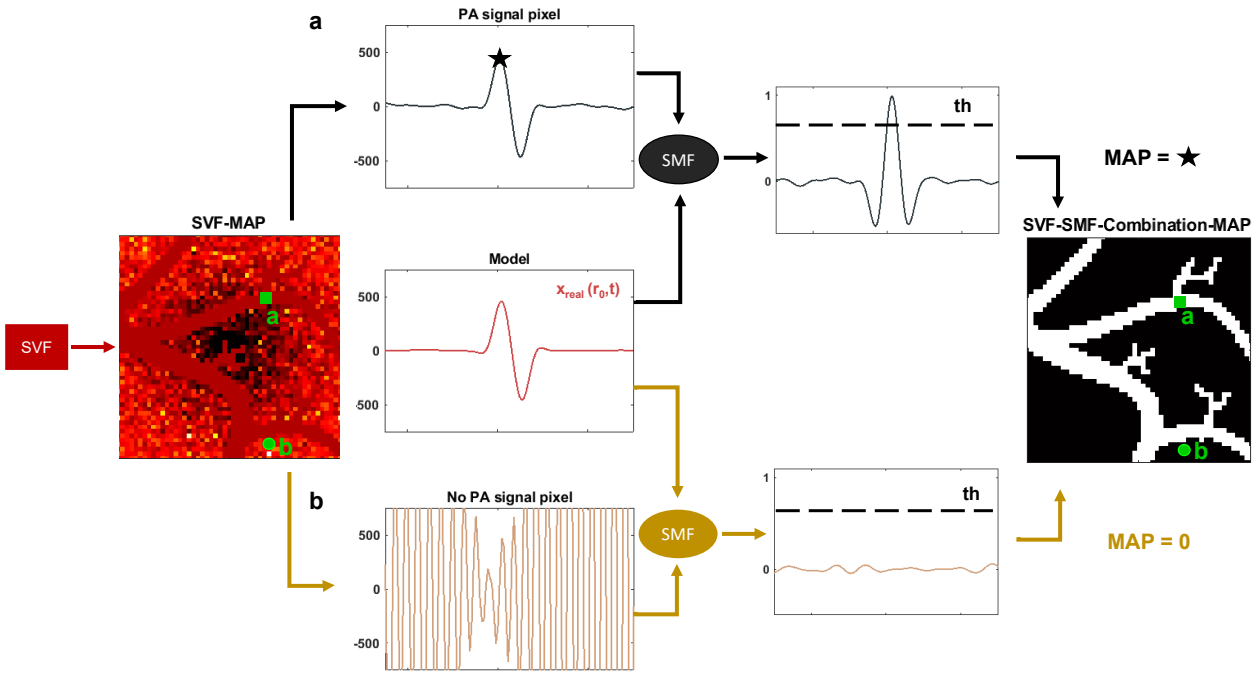

Figure 4.21: Workflow scheme for the proposed algorithm. It shows the process of obtaining the final MAP value for both a) signal and b) non-signal pixels.

The proposed algorithm is finally tested with a lateral gradient intensity profile to assess its performance, as depicted in Fig. 4.22. A faithful image is obtained thanks to the use of the SVF algorithm, with the addition of the improved homogeneous SNR that the SMF algorithm provides. As seen before, this would not be possible by the application of the algorithms separately, which offers a new path to achieve the objective of having larger imaging areas while maintaining a competitive image quality.

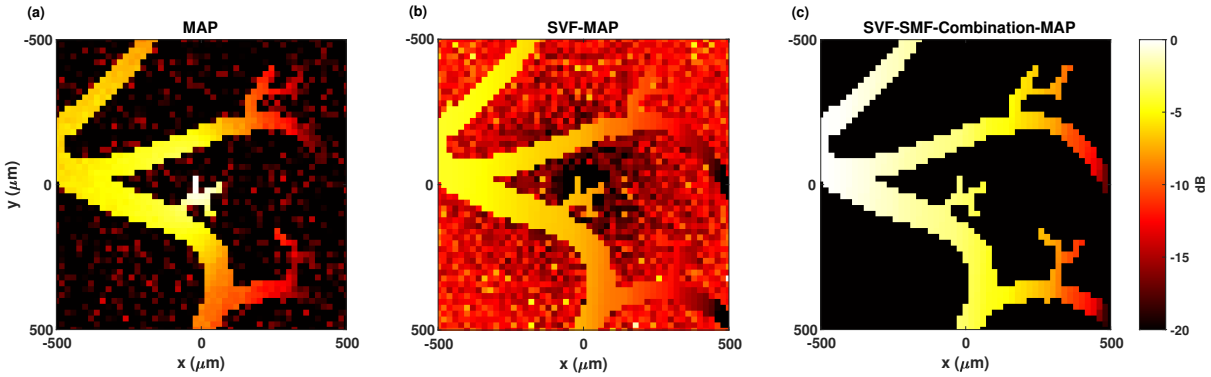

Figure 4.22: MAP images of the a) non-compensated image, b) compensated image using the Spatially-Variant Filter, and c) compensated image using the SVF-SMF combination algorithm.

With this final analysis, it has been proven that the proposed combined algorithm fixes the drawbacks of the previously selected algorithms and thus, it can be proposed as a good candidate for the implementation of the FOV enlargement in a real OR-PAM system. In consequence, this

compensation algorithm will help to build an OR-PAM prototype system based on a fast laser scanning and reduced acquisition times, as well as high quality images of high SNR, using low energy and low-cost lasers like the PLDs, which could be eventually translated into a feasible clinical practice.

Chapter 5

Conclusions and future work

This Master's Final Thesis has been carried out within the frame of a research project for developing a low-cost optical resolution photoacoustic microscope for subcutaneous imaging and melanoma diagnosis. The design of the OR-PAM prototype is based on a previous experimental system based on low-cost power laser diodes (PLD). However, it was limited to very slow image acquisition times due to its mechanical scanning, low SNR and image contrast, due to the low transducer sensitivity of a linear array probe used in this system (García-Garrigós et al., 2023). These two main drawbacks needed to be improved in the prototype design in order to open the possibility for future clinical applications with fast and high quality photoacoustic images from 2 to 4 mm under the skin. In this work, these two main problems have been tackled: a new design of a focused transducer with high sensitivity and the simulation study under realistic conditions for the implementation and evaluation of impulse response-based algorithms for enlarging the field of view limited to the acoustic focus.

To accomplish these objectives, an initial study of ultrasound radiation theory has been performed using the Rayleigh-Sommerfield model. Moreover, an optimization process to obtain the best geometrical configuration of the transducer that allows a high reception gain within the biggest possible acoustic focus was also carried out. The final transducer design had an active element of 60 mm and focal length of 30.25 mm ($f_{\#} \simeq 0.5$), yielding to a total active surface of 38.2 mm^2. This guarantees a substantially greater sensitivity when compared to unfocused and focused detectors with small active areas. For the transducer frequency response selection, a photoacoustic simulation platform in MATLAB named *k-wave* has been used to study the effect of spatio-temporal laser excitation parameters in the PA signal such as the pulse duration or the beam size. This was carried out in order to ensure the frequency match between the generated PA signal and the available transducer bandwidth, hence maximizing the reception sensitivity. A final bandwidth from 2 to 13 MHz at 6 dB has been selected following the obtained results and manufacturer specs.

Once the transducer design is done, it has been introduced into *k-wave* for performing an evaluation of three algorithms based on the spatial impulse response (SIR) of the transducer, aiming to enlarge the limited image field of view beyond the acoustic focus. The SIR was

obtained for an image area of 1x1 mm, and used to compensate the reduced sensitivity out of the acoustic focus. It has been proved that this methodology fully compensates images in a range of 1x1 for the first time, an order of magnitude greater than the sensitivity field of the transducer.

The algorithms performance was tested with as realistic as possible conditions, using a pixelated mask of absorbers emulating a vein network (vein phantom), and afterwards, adding Gaussian noise of 10 dB of Signal-to-Noise-Ratio (SNR) to the image for robustness evaluation on a less favorable scenario. It has been shown that the Spatially-Varying Filter (SVF) and Spatial Matched Filter (SMF) compensate the influence of the geometry, but with the addition of some drawbacks. The SVF decreases the SNR in pixels without PA signal, although it faithfully compensates the signal distortions. On the contrary, the SMF tends to binarize the final image since it acts like a detection algorithm, but it improves the final SNR since the noise is completely removed by thresholding. On the other hand, the Weighted Back-Projection (WBP) does not provide a full compensation. In addition to the performance evaluation, a new algorithm has been proposed as a combination of the SVF and SMF algorithms, which provides an excellent performance with extremely noisy signals, thanks to the SMF ability of noise removal, obtaining high-SNR and high-contrast images, while also preserving the image fidelity, capturing the variation of intensity in each image pixel due to different photoacoustic excitation levels across the sample.

This work sheds light on new and clearer knowledge about the limitations and characteristics of PLD-based OR-PAM systems, since their characteristics greatly differ from high-cost scanners based on expensive solid state lasers. As future work, this research will continue with the experimental assembly of the designed transducer in the OR-PAM prototype, with the subsequent calibration tests of the whole system that will ensure a much better performance of the system compared to the previous generation. Moreover, the proposed algorithm will be implemented and tested in a real device for ensuring the correct compensation of low level signals out of the acoustic focus of the transducer that will allow photoacoustic images of large areas with fast laser scanning and, thus, very low acquisition times. After the prototype construction and validation tests, it is planned to obtain *in-vivo* images of melanoma in murine models, becoming the first group that accomplish real pre-clinical OR-PAM images with a low-cost set-up, enabling the accessibility of this technology to the daily clinical practice.

Bibliography

Agano, T., Singh, M. K. A., Nagaoka, R., & Awazu, K. (2018). Effect of light pulse width on frequency characteristics of photoacoustic signal–an experimental study using a pulse-width tunable led-based photoacoustic imaging system. *Int. J. Eng. Technol*, *7*(4), 4300–4303.

Andrés, D., Camarena Femenia, F., & Jiménez, N. (2022). Modelizando el campo acústico generado por superficies vibrantes. *Modelling in Science Education and Learning*, *15*(2), 5–23.

Araque Caballero, M. A. (2013). *Incorporating sensor properties in optoacoustic imaging* [Doctoral dissertation, Technische Universität München].

Beard, P. (2011). Biomedical photoacoustic imaging. *Interface focus*, *1*(4), 602–631.

Beissner, K. (2012). Some basic relations for ultrasonic fields from circular transducers with a central hole. *The Journal of the Acoustical Society of America*, *131*(1), 620–627.

Bell, A. (1880). On the production and reproduction of sound by light. *American Journal of Science*, *20*(118), 305–324.

Brown, R. B., Dufour, S., Deladurantaye, P., Le Bouch, N., Gallant, P., Méthot, S., Rochette, P. J., & Mermut, O. (2020). Effect of laser pulse shaping on photoacoustic dosimetry in retinal models. *Biomedical Optics Express*, *11*(11), 6590–6604.

Caballero, M. A. A., Rosenthal, A., Buehler, A., Razansky, D., & Ntziachristos, V. (2013). Optoacoustic determination of spatio-temporal responses of ultrasound sensors. *IEEE transactions on ultrasonics, ferroelectrics, and frequency control*, *60*(6), 1234–1244.

Chowdhury, K. B., Prakash, J., Karlas, A., Jüstel, D., & Ntziachristos, V. (2020). A synthetic total impulse response characterization method for correction of hand-held optoacoustic images. *IEEE transactions on medical imaging*, *39*(10), 3218–3230.

Dong, B., Li, H., Zhang, Z., Zhang, K., Chen, S., Sun, C., & Zhang, H. F. (2015). Isometric multimodal photoacoustic microscopy based on optically transparent micro-ring ultrasonic detection. *Optica*, *2*(2), 169–176.

Erfanzadeh, M., Kumavor, P. D., & Zhu, Q. (2018). Laser scanning laser diode photoacoustic microscopy system. *Photoacoustics*, *9*, 1–9.

Estrada, H., & Razansky, D. (2019). Model-based optical resolution optoacoustic microscopy. *Photons Plus Ultrasound: Imaging and Sensing 2019*, *10878*, 134–137.

Fang, C., Hu, H., & Zou, J. (2019). A focused optically transparent pvdf transducer for photoacoustic microscopy. *IEEE Sensors Journal*, *20*(5), 2313–2319.

Gao, F., Feng, X., Zhang, R., Liu, S., & Zheng, Y. (2017). Adaptive photoacoustic sensing using matched filter. *IEEE Sensors Letters*, *1*(5), 1–3.

García-Garrigós, J. J., Cebrecos, A., Navarro-Calvo, J. A., & Camarena, F. (2023). A fiber-coupled laser diode design for reflection mode optical resolution photoacoustic microscopy. *Ultrasonics*, *132*, 107008.

Hofmann, U. A., Li, W., Dean-Ben, X. L., Subochev, P., Estrada, H., & Razansky, D. (2022). Enhancing optoacoustic mesoscopy through calibration-based iterative reconstruction. *Photoacoustics*, *28*, 100405.

Jain, A., KJ, P., Sharma, A. K., Jain, A., & PN, R. (2015). Dielectric and piezoelectric properties of pvdf/pzt composites: A review. *Polymer Engineering & Science*, *55*(7), 1589–1616.

Jensen, J. A. (1997). Field: A program for simulating ultrasound systems. *Medical & Biological Engineering & Computing*, *34*(sup. 1), 351–353.

Jensen, J. A. (1999). A new calculation procedure for spatial impulse responses in ultrasound. *The Journal of the Acoustical Society of America*, *105*(6), 3266–3274.

Jensen, J. A., & Gori, P. (2001). Spatial filters for focusing ultrasound images. *2001 IEEE Ultrasonics Symposium. Proceedings. An International Symposium (Cat. No. 01CH37263)*, *2*, 1507–1511.

Jeon, S., Kim, J., Lee, D., Baik, J. W., & Kim, C. (2019). Review on practical photoacoustic microscopy. *Photoacoustics*, *15*, 100141.

Jiang, D., Chen, H., Zheng, R., & Gao, F. (2022). Hand-held free-scan 3d photoacoustic tomography with global positioning system. *Journal of Applied Physics*, *132*(7).

Li, L., Yeh, C., Hu, S., Wang, L., Soetikno, B. T., Chen, R., Zhou, Q., Shung, K. K., Maslov, K. I., & Wang, L. V. (2014). Fully motorized optical-resolution photoacoustic microscopy. *Optics letters*, *39*(7), 2117–2120.

Li, W., Hofmann, U. A., Rebling, J., Zhou, Q., Chen, Z., Ozbek, A., Gong, Y., Subochev, P., Razansky, D., & Deán-Ben, X. L. (2022). Broadband model-based optoacoustic mesoscopy enables deep-tissue imaging beyond the acoustic diffraction limit. *Laser & Photonics Reviews*, *16*(5), 2100381.

Lingvall, F., Olofsson, T., & Stepinski, T. (2003). Synthetic aperture imaging using sources with finite aperture: Deconvolution of the spatial impulse response. *The Journal of the Acoustical Society of America*, *114*(1), 225–234.

Lu, Q.-B., Liu, T., Ding, L., Lu, M.-H., Zhu, J., & Chen, Y.-F. (2020). Probing the spatial impulse response of ultrahigh-frequency ultrasonic transducers with photoacoustic waves. *Physical Review Applied*, *14*(3), 034026.

Lu, T., Wang, Y., Li, J., Prakash, J., Gao, F., & Ntziachristos, V. (2020). Full-frequency correction of spatial impulse response in back-projection scheme using space-variant filtering for optoacoustic mesoscopy. *Photoacoustics*, *19*, 100193.

Luo, X., Xiao, J., Wang, C., & Wang, B. (2021). Fast correction of "finite aperture effect" in photoacoustic tomography based on spatial impulse response. *Photonics*, *8*(9), 356.

Maslov, K., Stoica, G., & Wang, L. V. (2005). In vivo dark-field reflection-mode photoacoustic microscopy. *Optics letters*, *30*(6), 625–627.

Na, S., & Wang, L. V. (2021). Photoacoustic computed tomography for functional human brain imaging. *Biomedical Optics Express*, *12*(7), 4056–4083.

Passive cavitation detector datasheet - precision acoustics. (n.d.). https://www.acoustics.co.uk/wp-content/uploads/2022/03/PCD-TDS-v1-0222.pdf

Pi Martín, I. (2021). *Estudio numérico y experimental para evaluar el rendimiento de algoritmos de reconstrucción de imagen empleados en tomografía fotoacústica* [Master's thesis, Universitat Politècnica de València].

Seeger, M., Soliman, D., Aguirre, J., Diot, G., Wierzbowski, J., & Ntziachristos, V. (2020). Pushing the boundaries of optoacoustic microscopy by total impulse response characterization. *Nature communications*, *11*(1), 2910.

Shi, W., Hajireza, P., Shao, P., Forbrich, A., & Zemp, R. J. (2011). In vivo near-realtime volumetric optical-resolution photoacoustic microscopy using a high-repetition-rate nanosecond fiber-laser. *Optics express*, *19*(18), 17143–17150.

Song, K. H., & Wang, L. V. (2007). Deep reflection-mode photoacoustic imaging of biological tissue. *Journal of biomedical optics*, *12*(6), 060503–060503.

Tabaru, T. E., Hayber, S. E., & Saracoglu, O. G. (2018). Frequency domain analysis of laser and acoustic pressure parameters in photoacoustic wave equation for acoustic pressure sensor designs. *Current Optics and Photonics*, *2*(3), 250–260.

Treeby, B. E., & Cox, B. T. (2010a). K-wave: Matlab toolbox for the simulation and reconstruction of photoacoustic wave fields. *Journal of biomedical optics*, *15*(2), 021314–021314.

Treeby, B. E., & Cox, B. T. (2010b). K-wave: Matlab toolbox for the simulation and reconstruction of photoacoustic wave fields. *Journal of biomedical optics*, *15*(2), 021314–021314.

Turner, J., Estrada, H., Kneipp, M., & Razansky, D. (2014). Improved optoacoustic microscopy through three-dimensional spatial impulse response synthetic aperture focusing technique. *Optics letters*, *39*(12), 3390–3393.

Wang, K., Ermilov, S. A., Su, R., Brecht, H.-P., Oraevsky, A. A., & Anastasio, M. A. (2010). An imaging model incorporating ultrasonic transducer properties for three-dimensional optoacoustic tomography. *IEEE transactions on medical imaging*, *30*(2), 203–214.

Wang, L. V. (2008). Tutorial on photoacoustic microscopy and computed tomography. *IEEE Journal of Selected Topics in Quantum Electronics*, *14*(1), 171–179.

Weisstein, E. W. (n.d.). *Cross-correlation. from mathworld–a wolfram web resource.* https://mathworld.wolfram.com/Cross-Correlation.html

Wikipedia contributors. (2023). Gain–bandwidth product - Wikipedia, the free encyclopedia [[Online; accessed 26-June-2023]]. https://en.wikipedia.org/w/index.php?title=Gainbandwidth_product

Xia, J., Yao, J., & Wang, L. V. (2014). Photoacoustic tomography: Principles and advances. *Electromagnetic waves (Cambridge, Mass.)*, *147*, 1.

Xie, Z., Jiao, S., Zhang, H. F., & Puliafito, C. A. (2009). Laser-scanning optical-resolution photoacoustic microscopy. *Optics letters*, *34*(12), 1771–1773.

Yang, X., Stein, E. W., Ashkenazi, S., & Wang, L. V. (2009). Nanoparticles for photoacoustic imaging. *Wiley interdisciplinary reviews: nanomedicine and nanobiotechnology*, *1*(4), 360–368.

Yao, J., & Wang, L. V. (2014). Sensitivity of photoacoustic microscopy. *Photoacoustics*, *2*(2), 87–101.

Yuan, Y., Yang, S., & Xing, D. (2012). Optical-resolution photoacoustic microscopy based on two-dimensional scanning galvanometer. *Applied Physics Letters*, *100*(2).

Zeng, L., Liu, G., Yang, D., & Ji, X. (2013). Portable optical-resolution photoacoustic microscopy with a pulsed laser diode excitation. *Applied physics letters*, *102*(5).

Part II

Budget

Chapter 6

Budget

In this chapter, an economic estimation of this Master Thesis: "Design of a focused ultrasonic transducer and evaluation of impulse response compensation algorithms for an optical resolution photoacoustic microscope" is made. It contains the partial costs of the used materials and equipment, as well as the labor force costs. Finally, the total budget of the project is calculated.

6.1 Partial budget

6.1.1 Labor force costs

The development of this work involved the participation of a Master in Biomedical Engineering student, as well as two supervisors, which guided and corrected the project. The prices shown next in Table 6.1 are orientative, considering that a student receives 20 €/h. and the professional engineers and researches receive 40 €/h.

Table 6.1: Breakdown of the labor force costs of the people involved in the project development.

Description	**Unitary cost (€/ h)**	**Quantity (h)**	**Total cost (€)**
Biomedical engineer (student). Previous study and project development	20	600	12000
Physicist (supervisor). Supervision and project correction	40	100	4000
Telecommunications engineer (supervisor). Supervision and project correction	40	100	4000
		Total	**20000**

6.1.2 Inventoriable materials costs

The breakdown of the costs of the needed inventoriable materials to develop the current project is shown in Table 6.2, calculated by following the next equation:

$$\text{Cost}(€) = \text{Unitary cost } (€/\text{ u}) \cdot \text{Quantity (u)} \cdot \frac{\text{Use period (m)}}{\text{Amortisation period (m)}} \tag{6.1}$$

where u are the used units and m the months using the material, considering that a month has 30 days.

Table 6.2: Breakdown of the costs of the used inventoriable materials in the project development.

Description	Quantity (u)	Unitary cost (€/ u)	Amortisation period (years)	Use period (months)	Total cost (€)
LG Generic PC Intel-i7 3.4GHz 8GB RAM 1TB HDD	1	1190	10	10	99.17
Mathworks MATLAB student license 2022.b	1	69	1	10	57.5
				Total	**156.67**

6.2 Total budget

Finally, the total budget is shown in Table 6.3, where the direct costs shown above, as well as the IVA (21 %) and the indirect costs, which include the overhead costs (13 %) and the industrial profit (6 %) , usually assumed to be up to the 18 % of the direct costs, are included.

Table 6.3: Breakdown of the total costs of the project development.

Description	Cost (€)
DIRECT COSTS:	
Labor force costs	20000
Inventoriable materials costs	156.67
INDIRECT COSTS :	
(18 % of the direct costs)	3628.2
Partial budget	23784.87
IVA 21 %	4994.82
Final budget	**28779.69**